# Probing earthquake dynamics through seismic radiated energy rate: illustration with the M7.8 2015 Nepal earthquake

**Marine A. Denolle**[1]

[1]Department of Earth and Planetary Sciences, Harvard University

**Key Points:**

- Source spectrograms track the high-frequency radiation excited during earthquake rupture
- Radiated energy rate quantifies the temporal evolution of earthquake radiation
- Radiation is not uniform spatially and temporally, even in the simple rupture of the 2015 Nepal earthquake

Corresponding author: Marine Denolle, `mdenolle@fas.harvard.edu`

**Abstract**

Dynamic characterizations of earthquakes focus on whole-event representations, that is whether the total radiation of seismic waves is more or less energetic. *Denolle et al.* [2015] and *Yin et al.* [2018] suggest to use the source spectrogram in order to analyze the radiation during the rupture itself. Here, we take a retrospective view on these studies to better establish the methodology of source spectrogram, and highlight its strengths and limitations. We provide clear interpretation of the temporal evolution of the source spectrogram through time-variant high-frequency falloff rate and radiated energy rate using canonical kinematic and pseudo-dynamic examples. The radiated energy rate provides the amount of energy radiated through time and its integral is the total radiated energy. It is most sensitive to fault heterogeneities in the local slip-rate function and its peak, and in rupture velocity. The high-frequency falloff rate peaks at times of zero moment acceleration, but remains constant otherwise and theoretically equal to one. The M7.8 2015 Nepal earthquake exemplified the propagation of a slip pulse and is thus perfectly suited to demonstrate this approach. We use 3D empirical Green's functions to remove wave propagation effects and construct the P-wave source function. We then construct spectrograms and explore the variations in the radiated energy rate functions. We find that the Nepal earthquake radiated seismic waves at the beginning and at the end of the rupture, but not during the phase of high moment release. Finally, we interpret our results in light of rupture dynamics, i.e. the earthquake initiation, propagation, and arrest.

## 1 Introduction

The intensity of earthquake ground motions is mostly controlled by the earthquake source radiation. Understanding the mechanisms that control earthquake rupture is critical to accurately predict the ground motions of future earthquakes. The source of earthquakes is the occurrence of slip on a fault due to the drop of shear stress. The mechanics that controls how this process takes place not only affects the total slip, but also the spatial and temporal evolution of the slip. Two earthquakes can release the same moment, but their radiation may differ considerably; for instance a slow earthquake has lower seismic efficiency than a fast earthquake [*Kanamori and Rivera*, 2006]. Characterizing what controls the seismic radiation is vital for validating our understanding of the mechanics and to accurate ground motion prediction.

Conventional kinematic representations of earthquakes provide the evolution of slip on a fault. Knowledge of displacements are essential to characterize seismic hazards (i.e static stress transfer) in active tectonic regions. The kinematic inversion problem is intrinsically undetermined and yet we hope to resolve details on the fault with limited data. It provides either a smooth or an awkwardly heterogeneous source model from which any inference of earthquake physics, e.g. static stress drop, becomes dependent [*Ihmlé*, 1998; *Brown et al.*, 2015]. Choices often have to be made regarding the fault geometry, rupture velocity, and the parametrization of the local slip-rate function. Common functional forms of the slip-rate function are combinations of triangles [*Kikuchi and Kanamori*, 1991], or of cosine functions [*Ji et al.*, 2002], or of regularized Yoffe functions [*Tinti et al.*, 2005; *Galetzka et al.*, 2015]. Furthermore, the data is also regularized, either through bandpass filtering or through ad hoc combination of data types (long period surface waves, short period body waves, tsunami data, GPS data). Inferring dynamic properties from these models such as final stress change or drop [*Noda et al.*, 2013; *Brown et al.*, 2015; *Ye et al.*, 2016], frictional properties [*Tinti et al.*, 2005; *Galetzka et al.*, 2015], available energy [*Yin et al.*, 2017], and radiation efficiency [*Ye et al.*, 2016] trades off with inversion and data regularizations.

The dynamic representation of the earthquake is traditionally achieved through estimation of radiated energy. Unlike for the source kinematics, it does not require an inversion nor does it make any source parameterization. It only quantifies the kinetic energy carried by far-field seismic waves. The removal of 3D wave-propagation effects, in particular of seismic attenuation, is critical to accurately calculate radiated energy. The understanding of these long-range path effects is an endeavor of its own. Theoretical Green's functions require accurate and high-resolution global velocity and attenuation models and are often limited to low frequencies due to computational costs [*Nissen-Meyer et al.*, 2014]. Nearby small events can be used to construct an empirical Green's function (eGf), in which the 3D wave propagation effects are fully captured. But the eGf method requires knowledge of the small event source term to minimize biases brought by its own finite fault effects.

Once the path effects are removed, the body-wave displacement seismograms are proportional to the moment-rate function, which is the integral over the fault volume of all individual moment-rate functions. This function is often referred to as the Source Time Function (STF). The STF captures the release of moment; its duration is that of active fast slip; and its time integral is the seismic moment. The Fourier amplitude spectrum of the STF is introduced as the source spectrum, which is commonly estimated at local (*Abercrombie* [1995]; *Ross and Ben-Zion* [2016], among other studies), regional (*Shearer et al.* [2006]; *Kane et al.* [2013]; *Trugman and Shearer* [2017], among other studies) and at teleseismic distances (*Pérez-Campos and Beroza* [2001]; *Allmann and Shearer* [2009]; *Convers and Newman* [2011]; *Baltay et al.* [2014]; *Denolle and Shearer* [2016], among other studies). There are several ways to construct the STF. Kinematic inversions yield the STF by summing all inverted slip-rate functions over the fault plane [*Kikuchi and Kanamori*, 1991; *Ji et al.*, 2002; *Ye et al.*, 2016; *Hayes*, 2017]. Direct deconvolution of seismic waves from theoretical Green's functions gives an apparent STF (ASTF) that is specific to the source-receiver geometry that should average to the event STF. The SCARDEC method [*Vallée et al.*, 2011] uses global P and $S_H$ waves, the Rayleigh waves are also used in by the GCMT automated product [*Ekström et al.*, 2012], and the combination of all wave types potentially provides a broadband characteristic of the earthquake [*Ihmlé and Jordan*, 1995]. The deconvolution with an empirical Green's function is routinely done for source spectral studies (i.e. without the phase information) and has been employed to estimate ASTF in few regional studies [*Abercrombie et al.*, 2016; *Prieto et al.*, 2017].

The duration of the ASTF is greatly sensitive to rupture directivity effects and its azimuthal variation is routinely used to estimate these properties [*Haskell*, 1964; *Velasco et al.*, 1994; *Park and Ishii*, 2013; *Chounet et al.*, 2017]. In frequency domain, the corner frequency of the source spectrum is related to the ASTF duration and its azimuthal variation is used to provide rupture velocity (*Warren and Shearer* [2006]; *Kane et al.* [2013]; *Ross and Ben-Zion* [2016], among others). Discussion of the shape of the ASTF, however, is rather limited. Crack models predict an asymmetry in the STF shape [*Yoffe*, 1951; *Kostrov*, 1964; *Day*, 1982; *Ohnaka and Kuwahara*, 1990; *Tinti et al.*, 2005], which can be explained by a rapid drop in fault strength when modeled with slip weakening friction. Several studies have observed this asymmetry in the large earthquakes, but that the normalization of the STF to its duration still leads to a symmetrical STF [*Houston*, 2001; *Meier et al.*, 2017].

Variations in high-frequency radiation is expected from changes rupture velocity [*Spudich and Frazer*, 1984], which may result from fault geometrical complexity [*Adda-Bedia and Madariaga*, 2008; *Dunham et al.*, 2011; *Bruhat et al.*, 2016], and heterogeneity in fault properties such as pre-stress [*Das and Aki*, 1977; *Cochard and Madariaga*, 1994; *Huang et al.*, 2013], and frictional properties [*Madariaga*, 1983; *Guatteri and Spudich*, 2000; *Galvez et al.*, 2014]. Furthermore, near-fault inelastic material response is expected to absorb radiated energy and to deplete the radiation in high-frequency seismic waves [*Ma and Hirakawa*, 2013; *Roten et al.*, 2014, 2017]. Thus, rigorous observations of the spectrum of seismic radiation during the rupture is desired to validate our understanding of physical processes.

This study provides tools to identify whether or not seismic radiation is uniform or episodic throughout the rupture, in the hope to relate those episodes to physics. The temporal evolution of the source spectrum is in essence a spectrogram of the STF. We can parameterize it through its mean level (the STF itself), by the ratio of high-to-low frequency content as captured by the spectral high-frequency falloff rate, and by its integral over frequencies, which is essentially a measure of radiate energy rate.

The high-frequency falloff rate of source spectra has been inferred to vary along dip of subduction zones [*Ye et al.*, 2016]. In addition to this observation, several studies have indicated that low frequency radiation is promoted up-dip of faults in contrast to high-frequency radiation that is mostly representative of the down-dip excitation [*Yao et al.*, 2011; *Meng et al.*, 2011; *Yin et al.*, 2018]. Dynamic models of subduction-zone earthquakes also predict its along-dip variation [*Huang et al.*, 2013; *Kozdon and Dunham*, 2013; *Ma and Hirakawa*, 2013; *Galvez et al.*, 2014] where the slip-rate function in the down-dip part is enriched in high-frequencies compared to the shallow slip-rate functions. Thus an estimation of the variation in spectral falloff rate may be beneficial to infer properties of slip-rate functions within a rupture.

The radiated energy rate is basically seismic power and is proportional to the moment acceleration squared. Radiated energy rate has been used to quantify the low but spatially heterogeneous seismic efficiency of tectonic tremor [*Ide et al.*, 2008; *Yabe and Ide*, 2014]. Estimates of radiated energy rate for large teleseismic earthquakes have been proposed by *Poli and Prieto* [2016], through removal of theoretical attenuation model, and by *Denolle et al.* [2015] and *Yin et al.* [2018] through removal of eGfs. This study serves as a retrospective analysis of the work of *Denolle et al.* [2015] and *Yin et al.* [2018]. In these previous studies, we constructed a source spectrogram by windowing the far-field displacement seismograms, tapered by a Hanning window, and analyzed the evolution of the falloff rate and radiated energy in each time window. This work improves the methodology to construct the source spectrogram, analyzes the artefacts brought by data processing, and establishes the rigorous relationship between STF, radiated energy rate, and high-frequency falloff rates.

First, we build our intuition on a simple unilateral dislocation model [*Haskell*, 1964], then we artificially construct rupture heterogeneity using a statistical pseudo-dynamic model [*Mai and Beroza*, 2000; *Crempien and Archuleta*, 2015]. From these exercises, we find that tapering strongly affects the source spectrogram shape by imposing a spectral falloff (usually of slope 2) and significantly alters the radiated energy rate shape. The short time Fourier transform provides a robust estimate of radiated energy rate, with a slight bias toward under prediction of the total energy. Finally, we apply our method to the 2015 M7.8 Nepal earthquake, as a re-evaluation of *Denolle et al.* [2015]. We find that the Haskell model indeed describes particularly well the rupture, whereby seismic radiation occurs at the beginning and at the end of the rupture. This earthquake highlights the counter-intuitive seismic signature of earthquakes: large slip or moment release does not necessarily mean large seismic radiation.

## 2 Source spectrogram analysis using canonical source time functions

The removal of 3D wave propagation effects is to be treated separately and we assume a homogeneous medium in this section. Let the STF be a trapezoidal function, an canonical representation of a moving pulse [*Haskell*, 1964]. The local slip-rate function is a boxcar function of rise time $T_R$ and slip is active for a total duration $T_D$. The STF is thus the convolution of two boxcar functions. To provide a realistic case, we choose $T_D = 30$ s and $T_R = 10$ s, which is appropriate for large magnitude earthquakes.

With the simplicity of the trapezoidal function, we can build physical intuition. During the ascending ($t < T_R$) and descending ($t < T_D - T_R$) phases of the STF, the function is linear with time, $\dot{S}(t) \propto t$. During any short time window within those two phases, the STF is also a linear function of time. The Fourier transform ($FT\langle\cdot\rangle$) of a linear function has an amplitude spectrum that decays with frequency, $|FT\langle t\rangle| \propto 1/f$. We thus expect the spectrogram to have a spectral decay $f^{-1}$ (falloff of rate of 1) during the phases of slip acceleration and deceleration. Because the slopes of the growth and deceleration phases remain constant, we expect the spectrogram to remain constant and equal in both phases. The flat part of the STF must be characterized by no spectral amplitude, except at the DC component, which should equate the amplitude of the STF at those times. First, we validate our intuition by constructing the source spectrogram. We then analyze it in terms of temporal evolution of the high-frequency falloff rate and the radiated energy.

### 2.1 Building the source spectrogram

We construct the source spectrogram, by taking the amplitude of the short time Fourier transform (STFT) of the STF, $\dot{S}(t)$, over a running short window of length $T_W$,

$$\widehat{\dot{S}}_P(f,t) = \frac{1}{T_W}\int_{t-T_W/2}^{t+T_W/2} \dot{S}(\tau)\exp(-2\pi i f\tau)d\tau. \quad (1)$$

In the STFT, the accuracy of the spectrogram depends on the window length $T_W$. For a first example, we choose $T_W = 3$ s.

The STFT directly applied to time series is thought to produce spectral leakage, which can be minimized by tapering the short time windows with a taper function $w(\tau)$ of duration $T_W$,

$$\widehat{\dot{S}}_T(f,t) = \frac{1}{T_W}\int_{t-T_W/2}^{t+T_W/2} \dot{S}(\tau)w(\tau-t)\exp(-2\pi i f\tau)d\tau. \quad (2)$$

The Hanning and Hamming windows are a popular choice of tapers to stationary fields and to STFT (Fig. S1). However, the operation of tapering is effectively a convolution in time, or a multiplication in frequency domain, such that the spectral falloff of the taper is imposed on that of the spectrogram. *Kaimal and Kristensen* [1991] show that the Hamming function least affects the short time windows. Furthermore, they find that a normalization of the taper is required to preserve the original time series amplitudes. If $n_W$ is the number of points in the taper, the proper normalization is $w = 2w/n_W$ and then $w = w/\text{mean}(w)$.

Spectral leakage of the untapered STFT does not appear to affect this simple example (Fig. 1a). We also use a normalized Hamming taper window (Fig. 1b), which retrieves correct amplitudes at the DC component, but alters the spectral shape at higher frequencies. Other strategies can improve the time-frequency resolutions. *Tary et al.* [2014] review most of the methods that are popular to seismological applications, including the Stockwell transform [*Stockwell et al.*, 1996]. Applying the S transform to the theoretical example of this study reveals undesirable artefacts at low frequencies and a distortion of the spectral shapes (Fig. 1c).

In the following sections, we take practical considerations of STF extracted for M7+ (duration > 10 s) recorded at teleseismic distances (signal reliable up to 2 Hz) and vary the window length from 0.5 s to 10 s (half of the duration of the pulse) to construct the STF spectrogram.

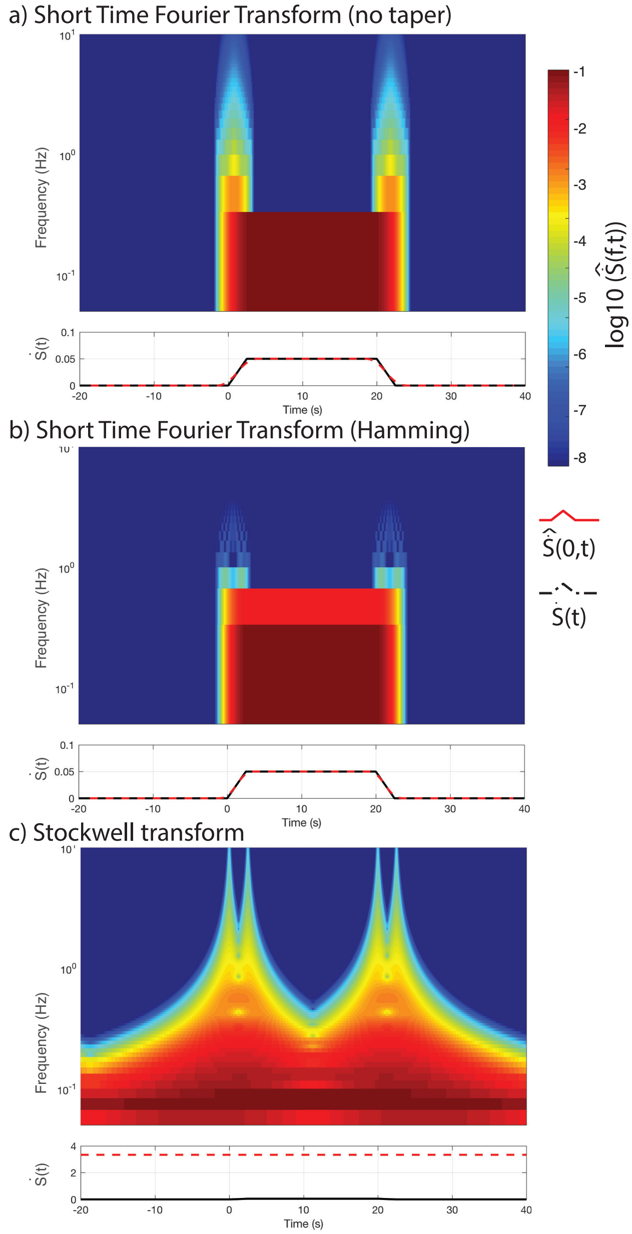


**Figure 1.** Spectrograms of the trapezoidal STF: STFT with a short window length $T_W = 3$ s without tapering (a) and with a Hamming taper (b), and c) the Stockwell transform. The first element of the STFT coefficient, $\widehat{\dot{S}}(0,t)$, is plotted against the theoretical STF $\dot{S}(t)$ in each bottom panels.

### 2.2 STF from spectrogram

A by-product of the STFT is that the first element of the spectrogram is the STF itself:

$$\widehat{\dot{S}}_P(0,t) = \frac{1}{T_W}\int_{t-T_W/2}^{t+T_W/2} \dot{S}(\tau)d\tau \quad , \tag{3}$$

$$= \frac{1}{T_W}\left[S(t+T_W/2) - S(t-T_W/2)\right] \tag{4}$$

$$= \dot{S}(t) \quad , \quad \text{if} \quad T_W \to 0 \tag{5}$$

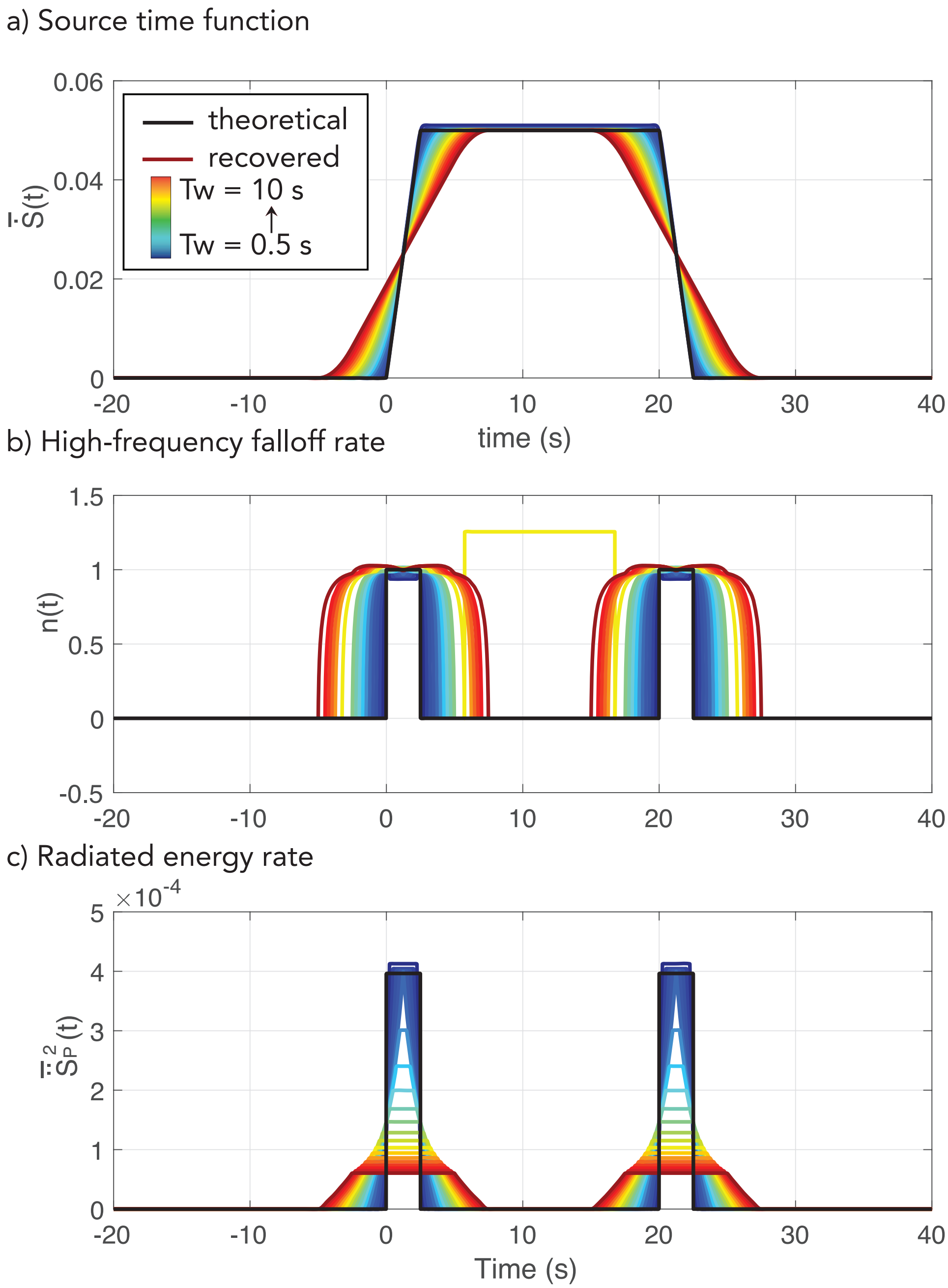


**Figure 2.** Parameterization of the source spectrogram: a) source time function, b) high-frequency falloff rate, c) radiated energy rate. All functions are normalized to a total slip value and thus denoted as $\bar{f}(t)$. The colorscale represents the window length $T_R$.

The example of the trapezoidal pulse shape is show in Figure 1 as the first element of the spectrogram. Figure 2(a) illustrates an obvious notion that short window lengths provide more accurate estimate of the STF than long window lengths. The long window lengths, in this case half the duration of the pulse, generate spurious signals that are ahead of the pulse and at after its end. Note that the integral under each estimate remains unity, thus moment is preserved through the STFT regardless of the choice of $T_W$.

### 2.3 Time evolution of falloff rate

A desirable parameter to extract from the source spectrogram is the evolution of the high-frequency falloff rate. In the case of a trapezoidal function, we expect the falloff to be 1 during slip acceleration and deceleration and not identifiable at other times. We estimate the falloff rate of the spectrogram $n(t)$ through a linear regression,

$$\log_{10}\left|\widehat{\hat{S}}_P(f,t)\right| = A(f,t) - n(t)\log_{10} f. \tag{6}$$

We are only interested in the asymptote of the spectral shape. The absolute level (shown as $10^{A(f,t)}$) is related, though not equal, to the slip (or moment). To balance the contribution between low and high frequencies in the regression, we interpolate $\left|\widehat{\hat{S}}(f,t)\right|$ onto an evenly log-spaced frequency vector. We use a linear least square maximum likelihood criterion to best fit $n(t)$.

Figure 2(b) illustrates the best fit $n(t)$ for various of window lengths. As expected, the falloff within the slip acceleration and deceleration is unity and is not defined at other times. Because long window lengths smear the source pulse, a spurious values of $n(t)$ appear for larger $T_W$, as expected. Note that tapering the short window provides a different value of the falloff (see Fig. S1, S2, S3, S8).

### 2.4 Radiated energy rate

Seismic radiated energy is the total kinetic energy carried by seismic waves. For body waves, the energy is calculated as the integral of energy flux over a sphere $\Omega_0$. The kinetic energy flux at a position on the sphere $(\theta,\phi)$ is proportional to the velocity seismogram squared $\dot{u}^2_{\theta,\phi}(t)$,

$$E_R = \oiint_{\Omega_0} \int_{-\infty}^{\infty} \rho\alpha \dot{u}^2_{\theta,\phi}(t)\,dt\,d\Omega, \tag{7}$$

$$= \int_0^{\infty} \dot{\varepsilon}(t)\,dt, \tag{8}$$

where $\alpha$ is the P wavespeed, $\rho$ is the density, and the radiated energy rate is:

$$\dot{\varepsilon}(t) = \rho\alpha \oiint_{\Omega_0} \dot{u}^2_{\theta,\phi}(t)\,d\Omega. \tag{9}$$

The far-field P-wave velocity seismogram is proportional to the time derivative of the STF, which we refer to as moment acceleration and denote $\ddot{S}(t)$, the radiation pattern $R_P(\theta,\phi)$, elastic properties and the distance $r$ [*Aki and Richards*, 2002],

$$\dot{u}_{\theta,\phi}(t) = \frac{R_P(\theta,\phi)}{4\pi\rho\alpha^3 r}\ddot{S}(t). \tag{10}$$

The integral over the sphere is $\oiint_{\Omega_0} d\Omega = 4\pi r^2$ and the fields that are averaged over it are noted as $\langle\cdot\rangle_{\Omega_0}$. The P-wave radiation pattern squared and averaged over the focal sphere is $\left\langle R_P^2(\theta,\phi)\right\rangle_{\Omega_0} = 4/15$. In practice, when we remove the path effects with an eGf, the radiation pattern term is already removed. Thus, we approximate the radiation pattern in equation (10) to be the focal-sphere average radiation pattern. We then write the radiated energy rate,

$$\dot{\varepsilon}(t) = \frac{2}{15\pi\rho\alpha^5}\ddot{S}^2(t). \tag{11}$$

Radiated energy rate is directly proportional to the moment acceleration squared. We find that in practice the moment acceleration as time derivative of the STF is not particularly stable (discussed in section 4.4) so that we turn to the source spectrogram to construct a robust estimate of the moment acceleration. The source spectrogram provides an estimate of the moment-rate spectrum at each time. The moment acceleration squared may be obtained from the source (moment-rate) spectrogram,

$$\ddot{S}_P^2(t) = \int_0^\infty \left|2\pi f \hat{\dot{S}}_P(f,t)\right|^2 df. \tag{12}$$

The relation above is validated for the Haskell model and shown in Figure 2(c) where we compare the theoretical acceleration squared with that retrieved from source spectrograms. It is worth noting that the spectrogram analysis systematically underpredicts the peak amplitudes of the moment accelerations.

At each station, we can estimate the radiated energy rate from the source spectrogram as:

$$\dot{\varepsilon}(t) = \frac{8\pi}{15\rho\alpha^5} \int_0^\infty \left|f \hat{\dot{S}}_P(f,t)\right|^2 df. \tag{13}$$

In practice, equation (13) is identical to estimating the total radiated energy from source spectra [*Baltay et al.*, 2010, 2014; *Denolle et al.*, 2015; *Denolle and Shearer*, 2016] except that it is calculated at each time step. To estimate the total P-wave radiated energy at each station, we simply integrate over time:

$$E^r = \int_0^\infty \dot{\varepsilon}(t)dt. \tag{14}$$

To validate that we can retrieve the total radiated energy from this source spectrogram method, we compare the theoretical energy $E_R$ with $E^r$. The data processing, e.g both short window length $T_W$ and the tapering method, affect the ability to recover $E_R$ from $E^r$ (Fig. 3).

Given a source duration of 30 s and teleseismic waves with good signal up to about 2 Hz, a reasonable choice for short window length may be between 2 s and 8 s. The estimate of $E^r$ from untapered STFT systematically underpredicts the true energy $E_R$ by 25%–40% and the tapered STFT provides about the right answer. While the taper function alters the spectral shapes, the total radiated energy remains almost unchanged with tapering. The loss in high frequency levels is compensated by the amplified low frequencies (Fig. 1b). This is likely why *Yin et al.* [2018] find a realistic value of total radiated energy.

We perform similar analysis using other canonical STF shapes, namely the Brune function (Fig. S2) and a regularized Yoffe function consistent with dynamic models proposed by *Tinti et al.* [2005] (Fig. S3). These other examples confirm our findings in this section. We conclude that the source spectrogram can provide the evolution of the high frequency radiation and of the radiated energy rate.

## 3 Source spectrogram from realistic kinematic models

A realistic STF may exhibit a more complex structure. *Meier et al.* [2017] highlight the overall consensus in teleseismic estimate of large M7+ STFs. Yet they notice their log-normal variance around smooth models, which emphasize the diverse shapes of the STF for large events. From a kinematic perspective, such sub-events can be prescribed as asperities of large moment release or high slip rate. Variations in rupture velocity also generate high frequency ground motions, and a heterogeneous distribution of rupture velocity can be specified. We turn to pseudo-dynamic models to build a realistic kinematic source [*Guatteri et al.*, 2004]. These kinematic models are statistical representation of distributions of slip, rise time, and rupture velocity that are consistent with dynamic ruptures. They are computationally efficient and are popular in deterministic ground motion prediction [*Graves and Pitarka*, 2016; *Wirth et al.*, 2017]. We use the kinematic source generator proposed by *Crempien and Archuleta* [2015] that compiles the statistical analysis of dynamic ruptures [*Liu et al.*, 2006; *Schmedes et al.*, 2010, 2013].

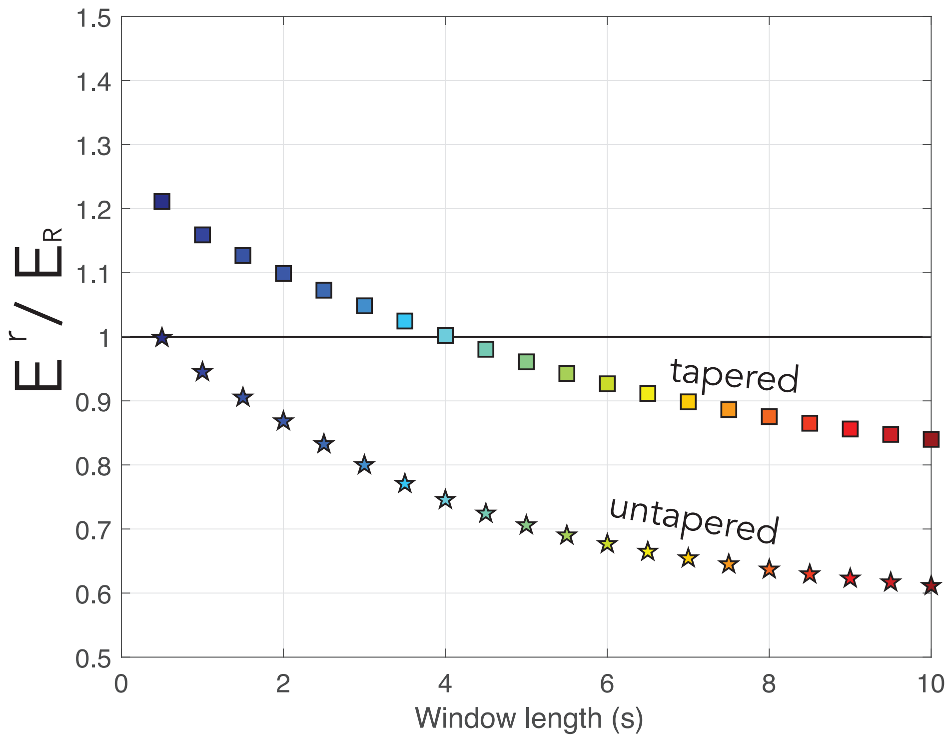


**Figure 3.** Ratio of the integrated radiated energy rate $E^r$ (equation 14) over total radiated energy $E_R$ as a function of window length $T_W$ (colorscale similar to Figure 2) for untapered SFTF (stars) and the tapered SFTF (Hamming taper, squares).

### 3.1 Kinematic source

In this example, we choose a source of magnitude M7.6, dimension 160 km × 18 km with a fault-averaged slip of 7.5 m. All spatial distributions are filtered by correlation length of 40 km, such that the distributions are somewhat smooth for wavelengths greater than the correlation length. The hypocenter is located half way along dip and on one end of the fault to simulate a simple unilateral rupture. The elastic properties chosen are that of a Poisson solid with $V_P$ = 5 km/s, $V_S = V_P/\sqrt{3}$, $\rho = 2,100$ kg/m$^3$. The rupture velocity is chosen approximately at 80% of the shear wavespeed $V_S$. We discretize the fault into 64 × 128 (8192) pixels of size 0.28 × 1.25 km. At each pixel, we impose a slip-rate function that takes the form of a regularized Yoffe function [*Tinti et al.*, 2005], with a ratio of slip acceleration time $T_{acc}$ to rise time $T_R$ of 0.5. The rise time $T_R$ is drawn from truncated Cauchy distributions and is correlated with slip and rupture velocity. The slip-rate function is scaled by taking its time integral and scaling it to the pixel slip (or moment for individual moment-rate function). The slip-rate function chosen is rather smooth and the falloff rate of this slip-rate function is of 3. Due to the scaling of the function with the slip (or moment) and its stretching to the local rise time, the peak slip rate increases with slip and with decreasing rise time.

The kinematic model we test is shown in Figure 4. The source has three main asperities with large slip (~ 10 m, Fig. 4a). The central asperity has peak slip rates (Fig. 4b) that are large and that probably over estimate true physical values. The spatial distribution of rupture velocities indicates that the rupture starts slowly in the first asperity, accelerates in the second asperity, and slows down in the third asperity.

From this kinematic model, we construct the normalized moment function, its rate, and its acceleration (Fig. 5a,b,c). We simply sum the contributions of individual slip-rate functions. It differs from observations of ASTF, whereby the observation is made at a particular point on the focal sphere (azimuth and takeoff angle). In our example, we do not analyze the effects of source directivity, which would alter the shape of the waveforms in Figure 5. However, we can test kinematic parameters that could control high frequency radiation: slip, peak slip rate, and variations in rupture velocity. The moment acceleration squared being proportional to the radiated energy rate, we also show the temporal evolution of radiated energy in Figure 5d. This example is interesting because it highlights a somewhat counter intuitive argument that seismic radiation is not necessarily a good measure for co-seismic slip: slip continues past 40 s, yet little energy is radiated. Additionally, a pulse duration estimate based on short period seismic waves would considerably underpredict the total event duration.

The times of most energetic radiation are mapped on the fault in Figure 4. The first peak of elevated energy occurs at about 7 s (Fig. 5d) and it colocates with a patch of high slip and slip rate (~15 km from epicenter). The second elevated peak in radiated energy occurs at a low slip/slip rate but at a change of rupture velocity (40 – 60 km along strike). The central asperity (60 –100 km along strike) excites more or less continuously high frequency waves, which results from a combination of high slip, slip rate and changes in rupture velocity. We conclude that slip only is not sufficient to explain elevated seismic radiation, but rather that slip, peak slip rate (through short rise time and high slip), and changes in rupture velocity all contribute to radiated energy. Of course, there is an ambiguity in these kinematic characteristics and a more rigorous analysis is beyond the scope of this study.

### 3.2 Source spectrogram analysis

The source spectrogram analysis of the kinematic source highlights interesting strengths and limitations of the method.

First, the functions derived from spectrograms converge toward the theoretical functions if $T_W$ is small. The first element of the spectrogram is the DC component (approximation of the STF, Fig 6a), and the second element of the spectrogram corresponds to the frequency $f = 1/T_W$. Thus, the shorter the window length is (small $T_W$), the higher and narrower the frequency band the spectrogram is sampled at. The spectrogram between the DC component and $f = 1/T_W$ ought to be almost linear for this approximation to hold and for the functions ($\dot{S}_P(t)$ and $\ddot{S}^2_P(t)$) to converge toward the theory. The fact that our approximation of the STF and its acceleration reproduces so well the theory may arise from little complexity in the source spectrogram at long periods.

Second, $\dot{S}_P(t)$ and $\ddot{S}^2_P(t)$ are effectively low-pass filter of the theoretical functions by the STFT (Fig. 6a,c). It is not unreasonable in practice to obtain smooth functions because other approaches adopt regularization in kinematic inversions and deconvolutions. A robust result is that the peak values of the $\dot{S}_P(t)$ and $\bar{\ddot{S}}^2_P(t)$ are lower bound values.

Finally, we conclude that the analysis of the high-frequency falloff rate is complicated and difficult to interpret. Unlike the example of the Haskell model in Figure 2, the temporal evolution of the falloff rate $n(t)$ is characterized by a median level at 1 and by narrow peaks. The rougher the STF, the more peaks appear in $n(t)$. Individual peaks in $n(t)$ correspond to changes in the slope of the STF and a reduction in $\bar{\ddot{S}}^2_P(t)$ as one can visually correlate in supplementary Figure S4.

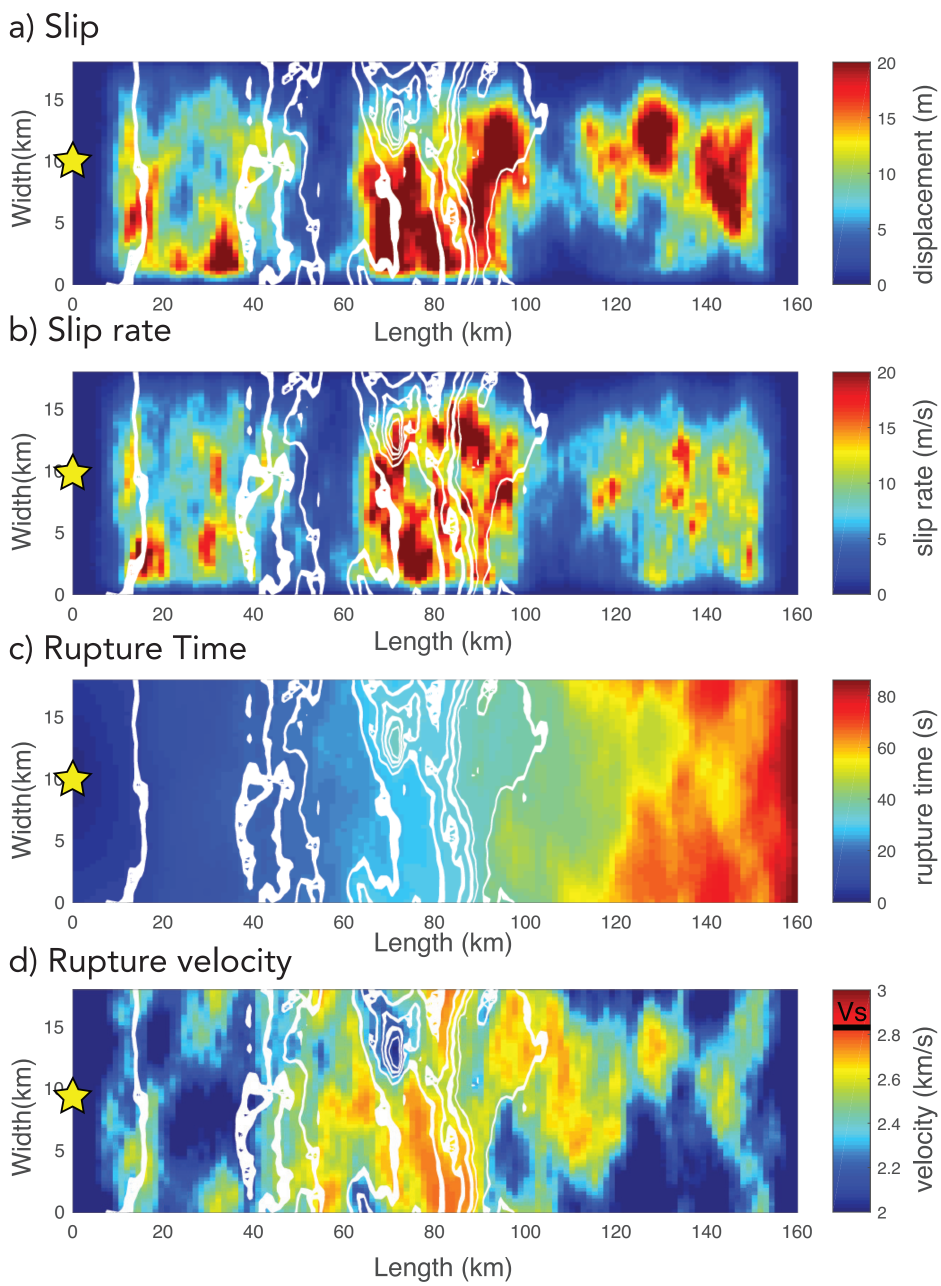


**Figure 4.** Distribution on the fault plane of kinematic parameters: slip (a), peak slip rate (b), rupture time (c), and rupture velocity (c). The yellow star indicates the hypocenter. The shear wavespeed $V_S$ is highlighted in the colorbar of (d). The white curves indicate the times at which a moment acceleration squared (normalized to total moment) exceed the threshold of 1.5E-4 as shown in Figure 5d.

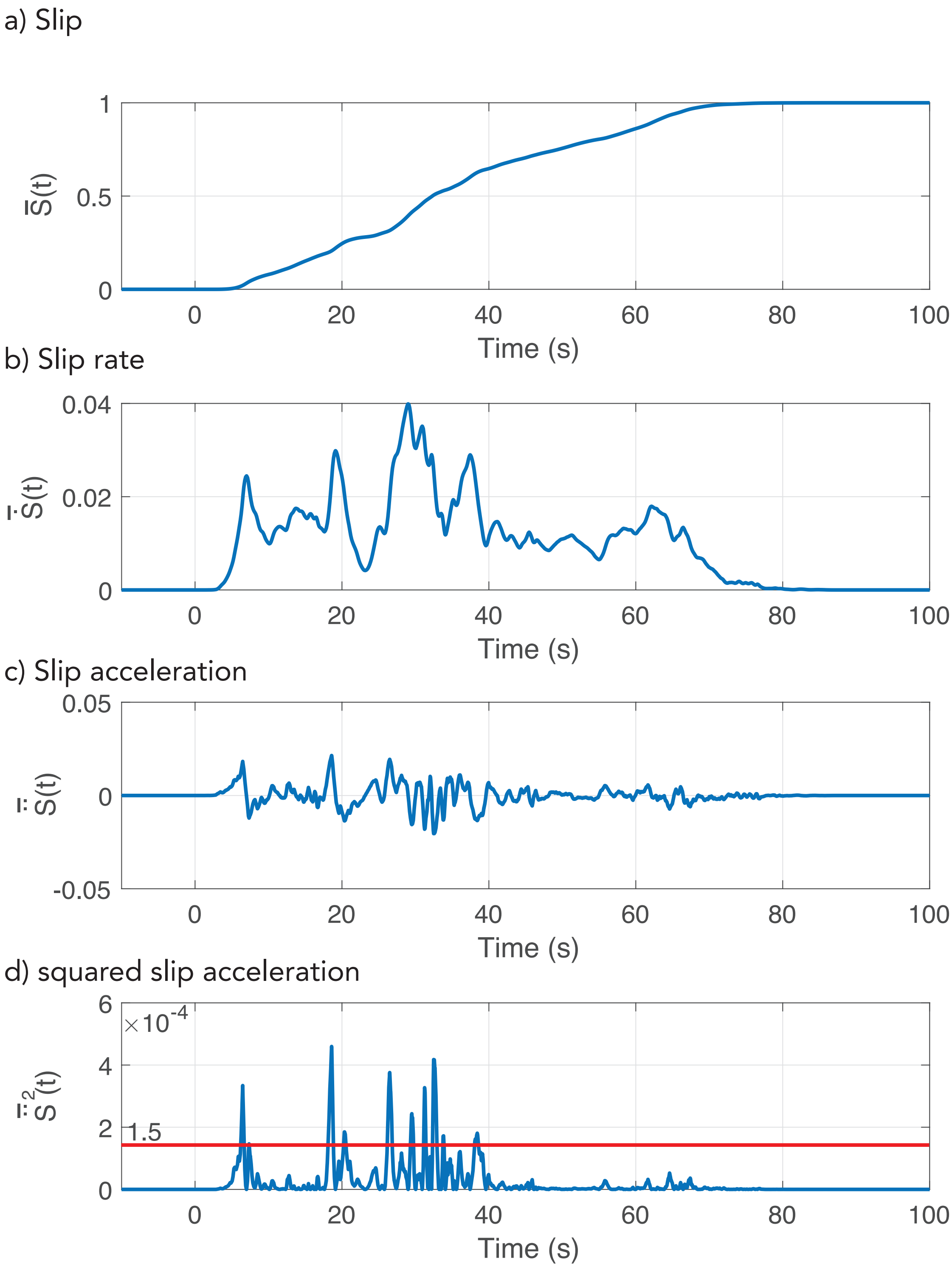


**Figure 5.** Fault-averaged slip function (a), slip-rate function (b), slip acceleration (c), and squared slip accelerations (d) all normalized to final slip with the convention $\bar{f}(t)$. The red line puts a threshold of the energetic peaks shown in Figure 4.

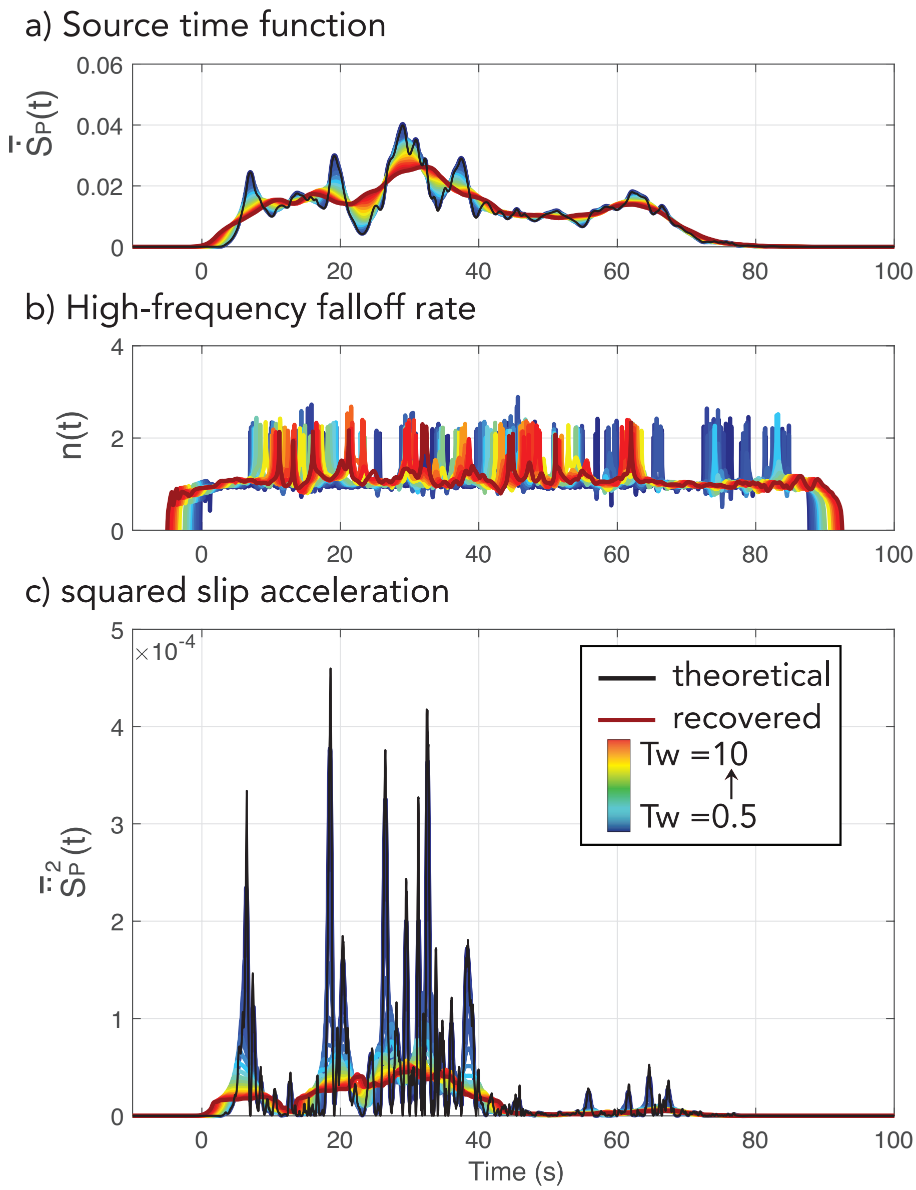


**Figure 6.** a) STF retrieved from the DC component of the spectrogram normalized to the final moment $\bar{\ddot{S}}^2_P(t)$, b) variations in high-frequency falloff rates, and c) slip acceleration squared normalized to the moment, similar to Figure 2. The colorscale represents the length of the short time window, from 0.5 s to 10 s. Black curves show the theoretical functions of the STF and normalized radiated energy rate $\bar{\ddot{S}}^2_P(t)$.

#### *3.2.1 Considerations on inhomogeneous slip-rate functions*

Along-dip variations in high frequency radiation are observed and may be explained by variations in the shape of the local slip rate functions, whereby the deep pulse is more impulsive than the shallow pulse [*Kozdon and Dunham*, 2013; *Ma and Hirakawa*, 2013; *Galvez et al.*, 2014; *Lotto et al.*, 2017].

This section aims to test whether we can detect a change in local slip-rate function in the source spectrogram. We artificially change the shape of the local slip-rate function from a symmetric pulse to an impulsive pulse (Fig. 7a). The tunable parameter is the ratio of the time to peak slip-rate, $T_{acc}$ to the rise time $T_R$. The impulsivity of the waveform is characterized by a shallow spectral falloff at high frequencies (Fig. 7b). We impose the sharper slip-rate function on the second half of the rupture, at along-strike distances 80 to 160 km from the epicenter. The total STF also has higher amplitudes at high frequencies and a shallower falloff between 1 Hz and 10 Hz (Fig. 7c).

We find that the change in slip-rate impulsivity during the rupture does not affect the high-frequency falloff rate. The second part of the rupture is characterized by a rougher falloff (see supplementary Figure S5), but not by a systematic change in the mean of the falloff rate. Instead, the impulsivity in the local slip-rate function greatly impacts the radiated energy. With a homogeneous slip-rate function, the second half of the rupture is characterized by significant slip (third asperity) but little radiation. The impulsive slip-rate functions instead promote radiated energy with levels that are greater at the end of the earthquake.

#### *3.2.2 Considerations on noise levels*

We explore the sensitivity of the high-frequency falloff rate and radiated energy to seismic noise. In particular for seismic stations located on Islands, often strategic locations to observe subduction zone earthquakes, the seismic noise is not white and has strong amplitudes at periods that approaches source durations (7 – 15 s, *Longuet-Higgins* [1950]). We choose ambient seismic noise from the station CI.CIA, which is located on the Catalinas Islands in southern California. We construct the noise time series by imposing the amplitude spectral shape of the realistic noise and adding a random phase. We vary the time-domain peak amplitude to model a signal to noise ratio from 0.01 to 1. The new time series have a distinct spectral shape before the synthetic STF (Fig. S6), thus a high-frequency falloff rate $n(t)$ exists before the event (Fig. S7). The radiated energy rate does not get significantly affected by the noise level.

We conclude that realistic seismic noise affects the interpretation of the high-frequency falloff rate at times prior and after the main pulse and that radiated energy rate remains robust with respect to the ambient seismic noise levels.

#### *3.2.3 Notes on tapering the STFT*

We examine the effects of tapering the short windows of the spectrogram in the kinematic source. We find that the variations of high-frequency falloff rate and radiated energy rates are particularly sensitive to the choice of tapers. The uniform taper is equivalent to no tapering, the Kaiser, Hamming, and Hanning tapers carry progressively stronger supressing of the amplitudes at the edge of the windows (see Fig. S1). We find that the stronger the taper (such as Hanning or Hamming), the greater the effects on both falloff rates and radiated energy. This exercise is shown in supplementary Figure S8. The temporal evolution of the falloff rate is leveled to that of the taper spectral decay: the Hanning taper has a spectral falloff of approximately 3 and thus the median falloff rate of the spectrogram is 3. Additionally, the shape of the radiated energy rate function is greatly affected: the stronger the taper, the more similarity the radiated energy rate function bears with the STF itself. In other words, the tapering amplifies the spectral levels at low fre-

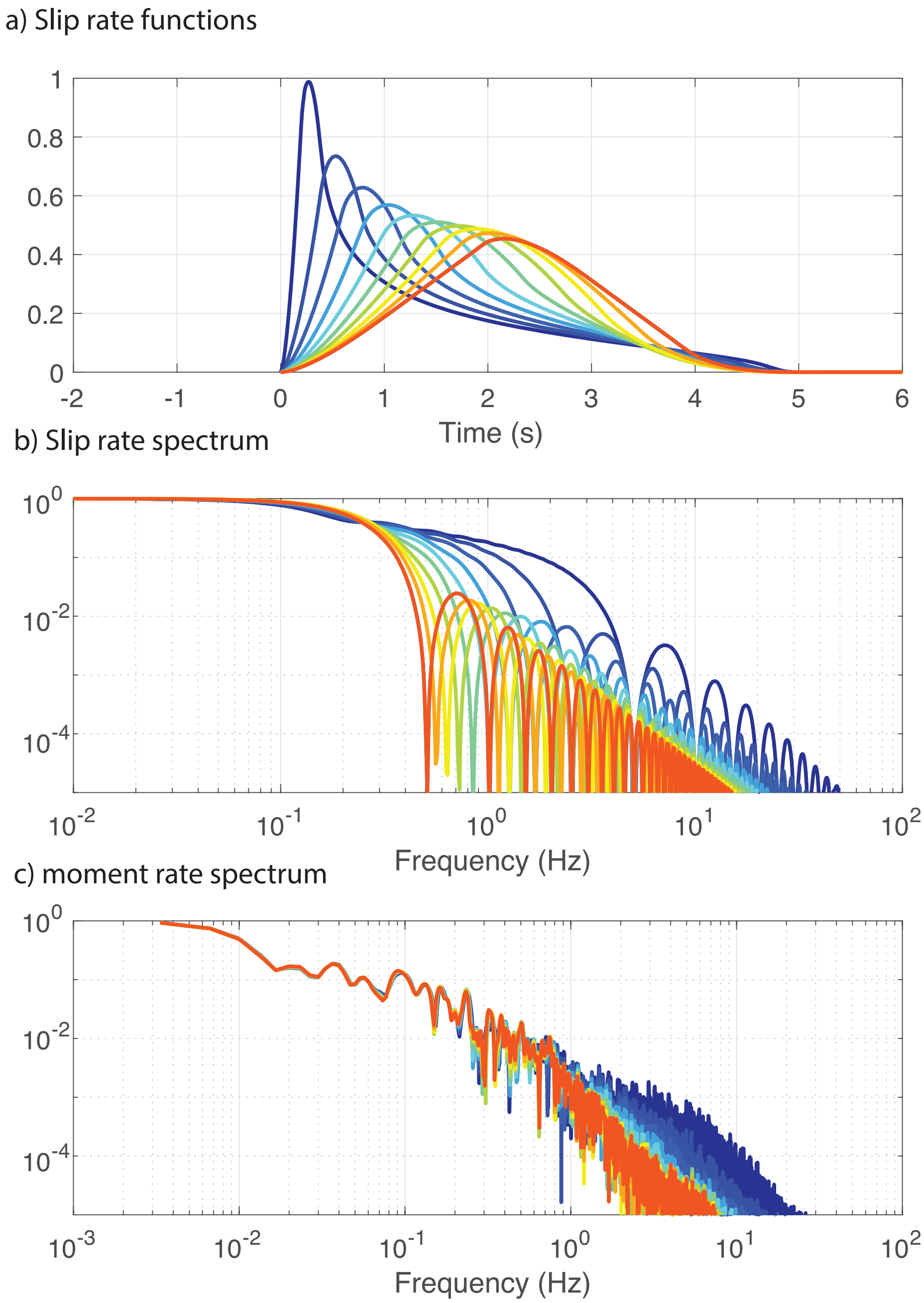


**Figure 7.** Individual slip-rate functions as regularized Yoffe function (a), their Fourier amplitude spectra (b), and the resulting kinematic source amplitude spectrum (c). The jet colorscale highlights the impulsive (blue) to symmetric (red) slip-rate function by increasing $T_{acc}/T_R$.

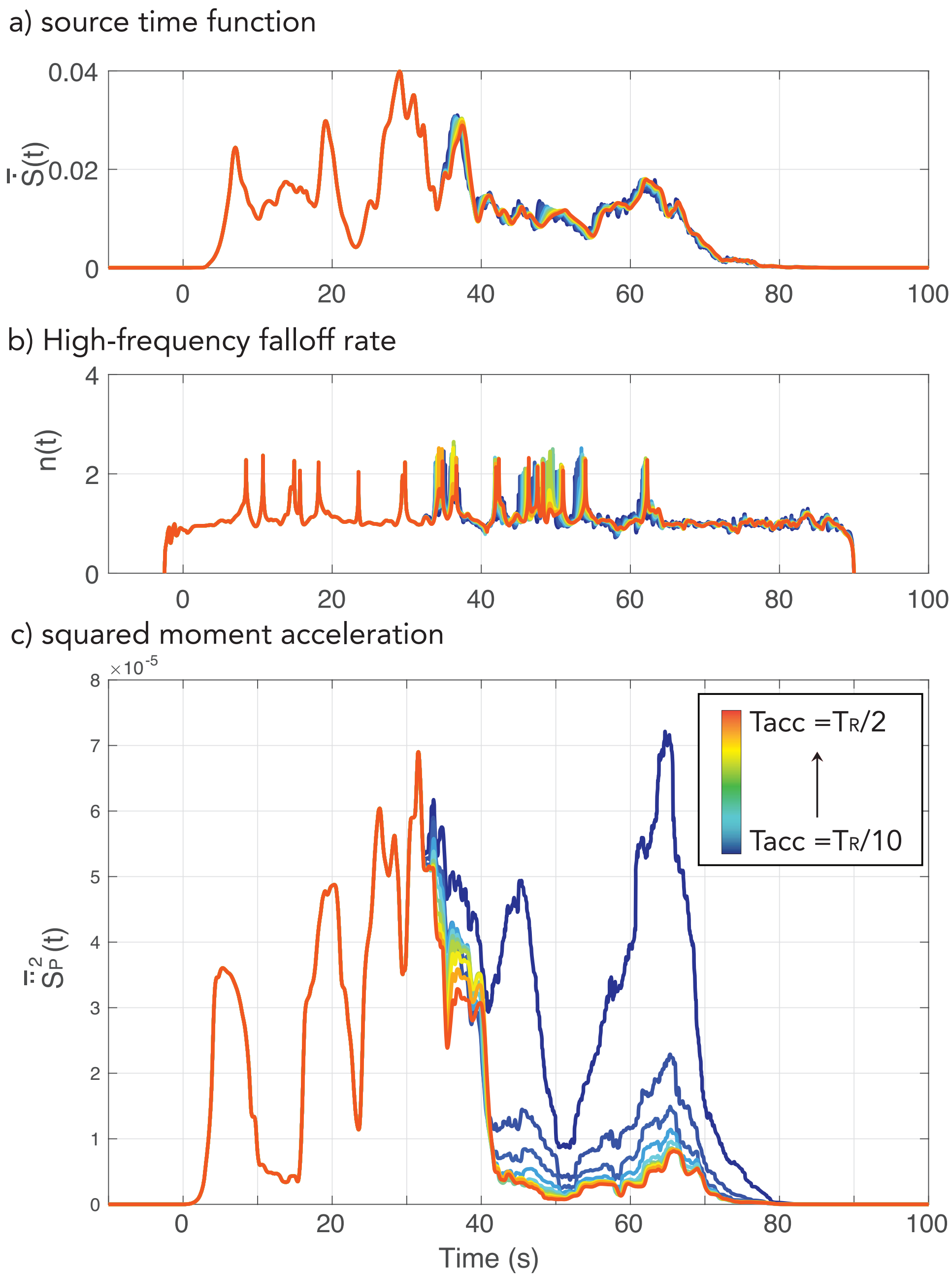


405 **Figure 8.** Effects of variations in local slip-rate impulsivity halfway through the rupture: (a) STF (ampli-
406 tude spectrum shown in Figure 7(c)), high-frequency falloff rate with time (b), and normalize radiated energy
407 rate (c). Colorscale similar to Figure 7.

quencies compared to the high frequencies, and thus provides a function that is more related to moment release (STF) than moment acceleration squared.

## 4 Application to the M7.8 2015 Nepal earthquake

The M7.8 2015 Nepal earthquake is particularly well suited to demonstrate the importance of radiated energy rate as a new observational tool. The event was a megathrust-style earthquake that ocurred on the Main Himalayan Thrust (MHT), and was recorded by a vast coverage of seismic stations. It exemplifies the moving source model of Haskell [*Haskell*, 1964] as a well developed unilateral rupture of a slip pulse (*Galetzka et al.* [2015]; *Fan and Shearer* [2015]; *Avouac et al.* [2015] among many others). Its aftershock sequence also includes two large shocks, the April 26, 2015 M6.8 and the May 12, 2015 M7.3 events. The earthquake sequence is relatively shallow, and the Earth' surface body-wave reflections (pP and sP depth phases) present a challenge for interpreting the P-wave source pulse. We have analyzed this earthquake sequence in previous work [*Denolle et al.*, 2015; *Denolle and Shearer*, 2016] and are now improving upon these studies.

### 4.1 Data selection

We window the P wave for 220 s, including 10 s on each edge of the window where we apply a 10-s cosine taper on either end of the time series. The P-wave arrival time is estimated from a IASP91 global velocity model [*Kennett and Engdahl*, 1991] using the TauP software for each source-receiver pair [*Crotwell et al.*, 1999]. Raw velocity waveforms are downsampled to 20 Hz. Removing the instrumental response is not necessary because it disappears during the deconvolution of the two seismograms in the eGf approach that we employ.

A first level of data selection is performed by comparing the signal to noise level. In this step, we construct the amplitude spectra of the P waves and of a noise window, which we select as being 220-s long prior to the direct P-wave arrival time. We interpolate the amplitude spectra onto a logspaced frequency vector between 0.05 Hz and 5 Hz. The criterion is that the mean of the amplitude spectral ratio has to exceed 5. The interpolation on a logspaced vector heightens the contributions of the low frequencies, which are often better resolved than high frequencies due to our understanding of seismic attenuation. The stations selected must meet this criterion at all three events (main event and the two aftershocks).

Because high frequencies contribute greatly to radiated energy, we further select only stations that meet the following criterion: spectral ratios have to exceed a factor of 10 above 1 Hz. We keep the signals up to a maximum frequency that is between 1 Hz and 2 Hz depending on what maximum frequency met this criterion at all three events. This further reduces the data set down to 200 stations from an original data set of 482 stations.

To account for differences in the direct P-wave arrival time between the globally symmetric IASP91 model and the true 3D velocity structure, we re-align the waveforms. The cumulative integration of the raw seismograms provide displacement seismograms, which we normalize to their peak amplitudes for Figures 9 (main event) and S9 (aftershocks). For each event, the median of the normalized displacement waveforms serves as a reference seismogram to which we align all individual waveforms through cross-correlation phase measurements. Note that we flip the polarity of the waveforms depending on the polarity of the first second of the P waves.

### 4.2 Removing 3D path effects

We use an empirical Green's function approach to remove 3D wave propagation effects. It is particularly crucial for shallow earthquakes where depth phases (pP, sP) arrive

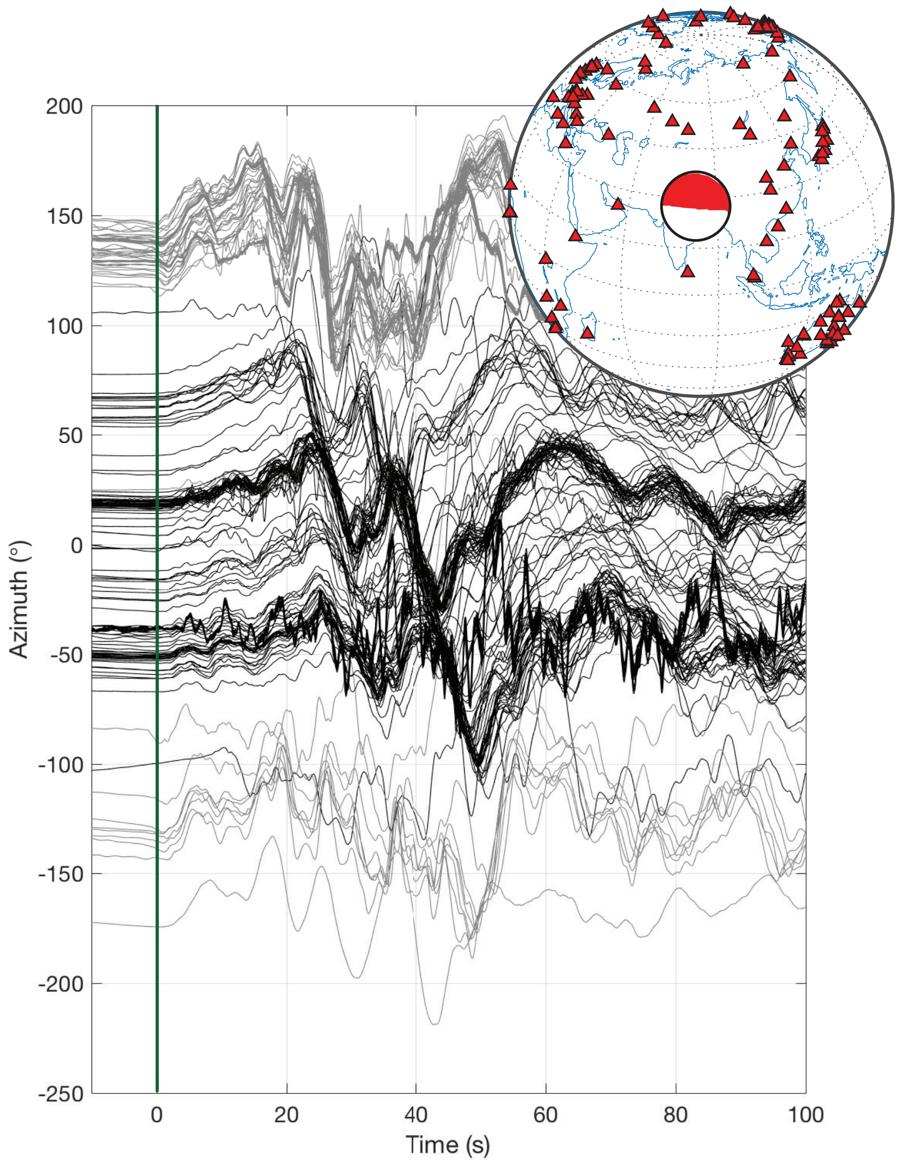


**Figure 9.** Normalized P-wave displacement waveforms recorded at the 200 stations used in this study for the M7.8 of April 25, 2015, Nepal earthquake. Waveforms are normalized to their peak absolute amplitudes. Black waveforms have positive direct P polarities while gray waveforms have negative (but flipped) polarities. Insert map shows the CMT mechanism and location of the stations.

soon after the direct P phase, before the end of the source pulse. Two aftershocks of the Nepal event occurred nearby the end of the active slip zone, the M6.8 of April 26 and the M7.3 of May 12 2015. At each receiver in the far field, the seismogram is the convolution of an earthquake source pulse, the moment rate function, $\dot{S}(t)$, and a propagation term that accounts for radiation pattern of a double-couple source and the spatial derivatives of the Green's function [*Aki and Richards*, 2002], which we note $G(t)$ for simplicity: $U(t) = \dot{S}(t) * G(t)$. Ideal empirical Green's functions are those constructed from small events nearby the target earthquake such that both share a similar radiation pattern and source-receiver path. The practical definition of attributes such as "nearby" [*Kane et al.*, 2013] or "similar" [*Abercrombie*, 2015] may influence our results, but the two eGfs are within a source dimension of the main shock, and their similarity is difficult to assess because the two eGfs have their own particular STFs.

To avoid biases in the estimate of the large pulse, the eGf event has to be small so that the STF of the small event, $\dot{S}_e(t)$, resembles a delta function compared to the STF of the target event. Because time-domain convolutions turn into frequency-domain multiplications, it is practical to write and construct the STF as,

$$\widehat{\dot{S}}(f) = \frac{\widehat{U}(f)}{\widehat{U}_2(f)} \widehat{\dot{S}}_e(f). \tag{15}$$

We apply a smoothing function (running average over 5 points) of the amplitude spectrum on $\widehat{U}_e(f)$ (not the phase) as it provides a more stable result. The choice of a simple smoothing function as against a multitaper approach [*Prieto et al.*, 2009, 2017] seeks to minimize data processing steps and the choice of their parametrization.

As the use of body-wave eGf at teleseismic distances is becoming more popular [*Ide et al.*, 2011; *Baltay et al.*, 2014; *Denolle and Shearer*, 2016], they have thus far focused on Fourier amplitude spectra and have ignored the phase information. Here, we keep both real and imaginary parts of the complex spectra and perform a simple deconvolution to recover both phase and amplitude information. Note that there are other methods to regularize the deconvolution of equation (15), such as that discussed in *Bertero et al.* [1997] and implemented by *McGuire* [2004]. We have tested conventional regularization using a water level and the implementation of *McGuire* [2017] but found that our simpler processing provided more stable results, which could be explained by a large amount of data (stations and eGfs) used in this study.

Because the aftershocks are relatively large, we need a model of $\widehat{\dot{S}}_e(f)$ as it no longer represents a delta STF compared to the main event. *Denolle and Shearer* [2016] solves for a model of $\widehat{\dot{S}}_e(f)$ for both aftershocks. They propose a double-corner frequency model as a best-fit model for the station-averaged P-wave spectra,

$$\widehat{\dot{S}}_e(f) = \frac{M_e}{\sqrt{(1 + (f/f_1)^2)\,(1 + (f/f_2)^2)}}, \tag{16}$$

where $M_e$ is the seismic moment of the small events ($M_e$=1.808E+19 Nm, 8.971E+19 Nm for the M6.8 and M7.3 respectively), $f_1$ is a low corner frequency that likely represents source duration and $f_2$ a high corner frequency that could represent the rise time $T_R$ [*Haskell*, 1964; *Denolle and Shearer*, 2016]. We choose the corner frequency found by *Denolle and Shearer* [2016] for the two eGfs, $f_1 = 0.0543, 0.0411$ Hz and $f_2 = 0.6194, 0.2182$ Hz for the M6.8 and M7.3 respectively. Choosing a single source spectrum for the eGf can bias the main event spectral estimates if the eGf is subject to source directivity [*Ross and Ben-Zion*, 2016], the raw waveforms shown in supplementary material (Fig. S9) does not visually exhibit strong directivity in the P-wavetrain pulses. We select stations that are between 20° and 98° of angular distance between the epicentral location and the receiver. The choice of incorporating stations at closer distances than 30° is that the eGf approach provides 3D path effects and thus is able to remove the effects of triplication of the P wave in the mantle. Because the P wavetrain contains depth phases (see Fig. 9 and

*Denolle et al.* [2015]), may contain triplications, and incorporates global reflection waves (PP), we only analyze the azimuthal variations in the P pulse rather than attempting to decompose it further in terms of takeoff angles.

For each station $i$, we construct a Green's function using the Fourier transformed raw seismograms of eGf1 ($\widehat{U}_i^1(f)$) and eGf2 ($\widehat{U}_i^2(f)$),

$$\widehat{G}_i(f) = \frac{1}{2}\left(\frac{\widehat{U}_i^1(f)}{\widehat{\dot{S}}_e^1(f)} + \frac{\widehat{U}_i^2(f)}{\widehat{\dot{S}}_e^2(f)}\right). \tag{17}$$

We find that this averaging is stable and provide further tests in supplementary materials Figure S10. Because our estimate of the Green's function is a linear stack of the individual Green's functions, the resulting STF is also an arithmetic mean of the STF estimated from individual eGf.

### 4.3 Apparent Source Time Functions

Removing path effects becomes a simple deconvolution of the raw seismograms with the Green's function $G_i(f)$,

$$\widehat{\dot{S}}_i(f) = \left(\frac{\widehat{U}_i(f)}{\widehat{G}_i(f)}\right)\exp(-2i\pi f T_1), \tag{18}$$

that we shifted by a time $T_1 = 50$ s for clarity of the onset of the STF. The STF at each station $\dot{S}_i(t)$ is thus the inverse Fourier transform of equation (18). We bin the STFs within azimuth bins of daz = 3.6° increment. Figure 10 shows the STFs as a function of time and azimuth.

Because we do not constrain non-negativity in the STF (no "back slip"), the individual ASTFs exhibit negative amplitudes at the beginning and end of the signal. At each azimuth, we remove the (negative) mean amplitude between $t$ = -5 s and $t$ = 5 s. An essential test to perform is to validate whether the moment-rate time integral equates a reasonable value of seismic moment. The seismic moment estimated from the average STF between 0 and 50 s and is $M_0$ = 4.5E+20 Nm, a value that is 57% of the GCMT estimate $M_0^U$ = 7.76E+20 Nm (M7.8 USGS), similar to that found by *Yue et al.* [2017] ($M_0$=6.4E+20 Nm, M7.8), and about half of that found by the SCARDEC database ($M_0$= 9.6 E+20 Nm, M7.9, scardec.projects.sismo.ipgp.fr, last accessed 02/21/18). There is an azimuthal variation of these estimates but it can be explained by the late noise in the STFs in the azimuthal range 50° – 120 °. Our moment estimate corresponds to a moment magnitude of 7.7.

The first remarkable aspect of the ASTFs is that source directivity is clearly visible with short pulses at azimuths between 80° and 120°, which is a rupture direction consistent with independent observations from back-projection [*Fan and Shearer*, 2015; *Yagi and Okuwaki*, 2015; *Galetzka et al.*, 2015; *Yin et al.*, 2017], kinematic source inversion [*Avouac et al.*, 2015; *Lay et al.*, 2017; *Yue et al.*, 2017], and teleseismic surface-wave source time functions [*Duputel et al.*, 2016]. A second noticeable aspect of the STFs is that there is little moment released in the first 10 s of the event, which has been observed and interpreted as a long slip initiation [*Denolle et al.*, 2015]. The slow initiation is clear on the direct P waves of the main shock (Fig. 8) and of the M6.8 aftershock (Fig. S9), which *Denolle et al.* [2015] suggested being an atypical slip nucleation process that is common to both M7.8 and M6.8 events. Lastly, the STF shape clearly varies with some azimuths (100° – 150°) exhibiting a single pulse, while other at azimuths (-40° – 50°) it is composed of two distinct pulses.

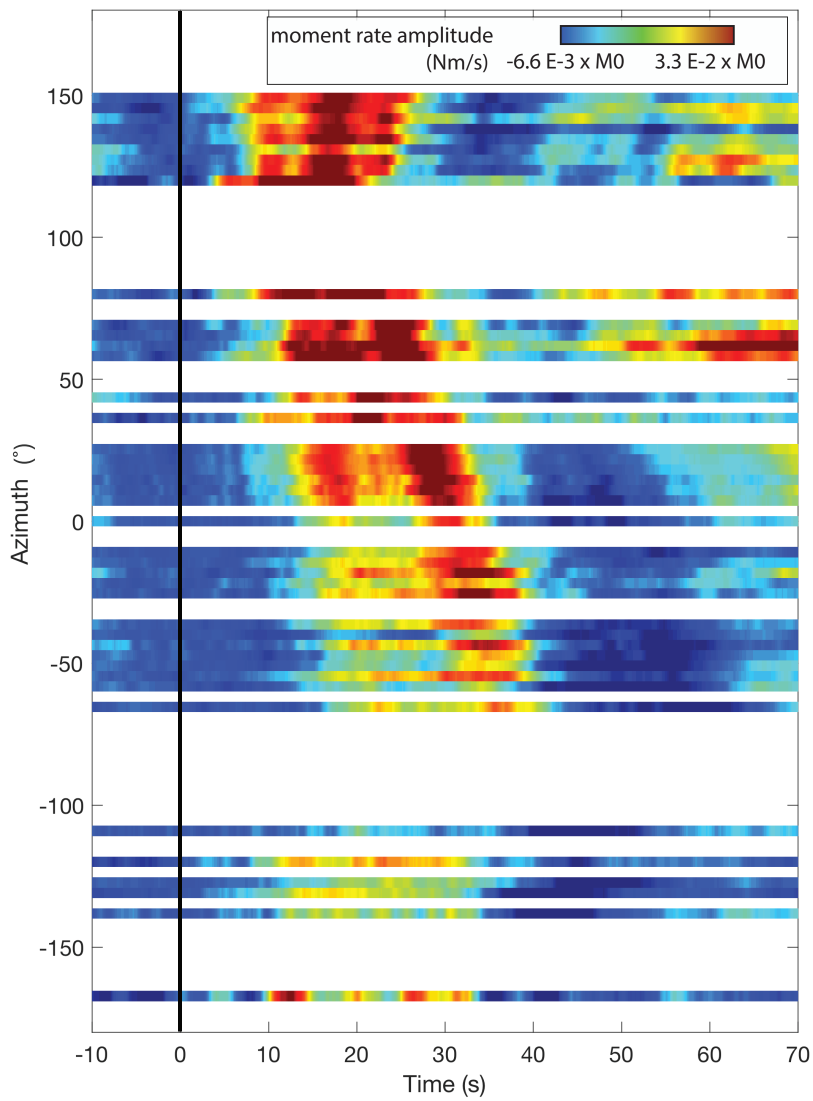


**Figure 10.** Whole event source functions (STF) in time domain sorted by azimuth, where data is available. Black line highlights the earthquake origin time in (a).

### 4.4 Radiated energy rate

We now proceed to constructing the radiated energy rate functions. We have explored the possibility of directly using the time derivative of the STF, squared, using a first order and a second order finite difference scheme. The lack of coherence between each azimuthal estimate of the acceleration squared (Fig. S14) lead us to use the spectrogram approach presented above, equation (13). At each azimuth bin, we estimate the spectrogram using $T_W = 5$ s and a Kaiser taper (with typical function parameter $\beta = 0.5$) from each azimuth-averaged STF. We remove the mean of the radiated energy function between $t$ = -20 s and $t$ = -10 s, thereby minimizing the acausal spurious seismic energy. As expected from the azimuthal variations in STF, the radiated energy rate is particularly inhomogeneous (Fig. 11).

The radiated energy rate is dominated by the starting and the stopping of the slip pulse: the onset is most energetic 10 s after the origin time and between 30 and 40 s of the event. Other features differ from a classic dislocation model of a unilateral rupture. First, it appears that the stopping phase is more energetic than the initiation phase. Second, certain azimuths exhibit intermediate peaks in high-frequency radiations, ones that are early after energetic slip initiation (azimuth range 120° – 150°), and ones that are preceding the slip deceleration (azimuth range -50° – 50°).

We revisit the results of *Denolle et al.* [2015] and *Yin et al.* [2018] and their choice of Hanning taper. The high-frequency falloff rates and radiated energy rate are particularly affected by the taper (Fig. 12). The amplitudes of the variations in falloff rates are enhanced by the tapering and this artifact should not be interpreted as a physical kinematic feature. Furthermore, the radiated energy rate functions are drastically different (Fig. 12b). The moment acceleration squared, scaled to the factor in equation (13), is shown as a theoretical reference. Given that the 2015 Nepal earthquake was remarkably similar to a Haskell model, the moment acceleration squared, and thus the radiated energy rate, must carry high amplitude at the beginning and at the end of the rupture. The use of weak tapers (uniform or Kaiser) yields radiated energy rate functions that are closer to the theoretical value. Intuitively, the strong tapers alter the spectrogram shape by enhancing the low frequencies and depleting the high frequencies, thus altering radiated energy rate function $\dot{\varepsilon}(t)$ to represent rather the source time function $\dot{S}(t)$. This effect is particularly evident in *Yin et al.* [2018]. Our analysis confirms that minimal tapering is the preferred data processing approach to retrieve radiated energy rate.

### 4.5 Comparison of the STF with other studies

Our spectral estimates bear strong similarities with *Denolle et al.* [2015]. In that study, we used a theoretical Green's function for the direct P-wave pulse and found similar azimuthal dependence in the spectral shapes. This frequency-domain view is not the scope of the paper and is only presented in the supplementary materials Figures S12 and S13.

We compare our median estimate of the STF against two other databases: SCARDEC [*Vallée et al.*, 2011] and USGS [*Hayes*, 2017] and find some differences between the three estimates (Fig. S15). We also compare their derived Fourier amplitude spectra and calculate the radiated energy from the STF, assumed to be equal to the P-wave pulse. The SCARDEC method estimates the moment to be almost twice as ours and thus it is reflected in the pulse amplitude and duration (Fig. S15). The USGS STF has a strong amplitude around 1 Hz, which greatly affects its estimate of radiated energy. Overall, our STF likely underpredicts the total moment by a factor of 2 and possibly the source duration by about 5 s. However, our estimate of radiated energy is more robust. If we assume that the S-wave pulse is identical to the P-wave pulse and that the geometrical spreading is controlled by the difference in elastic wavespeeds ($V_P = \sqrt{3} V_S$ ), we find an energy estimate from the SCARDEC STF of 4.2 E+16 J, that of USGS of 9.61 E+16 J, and ours

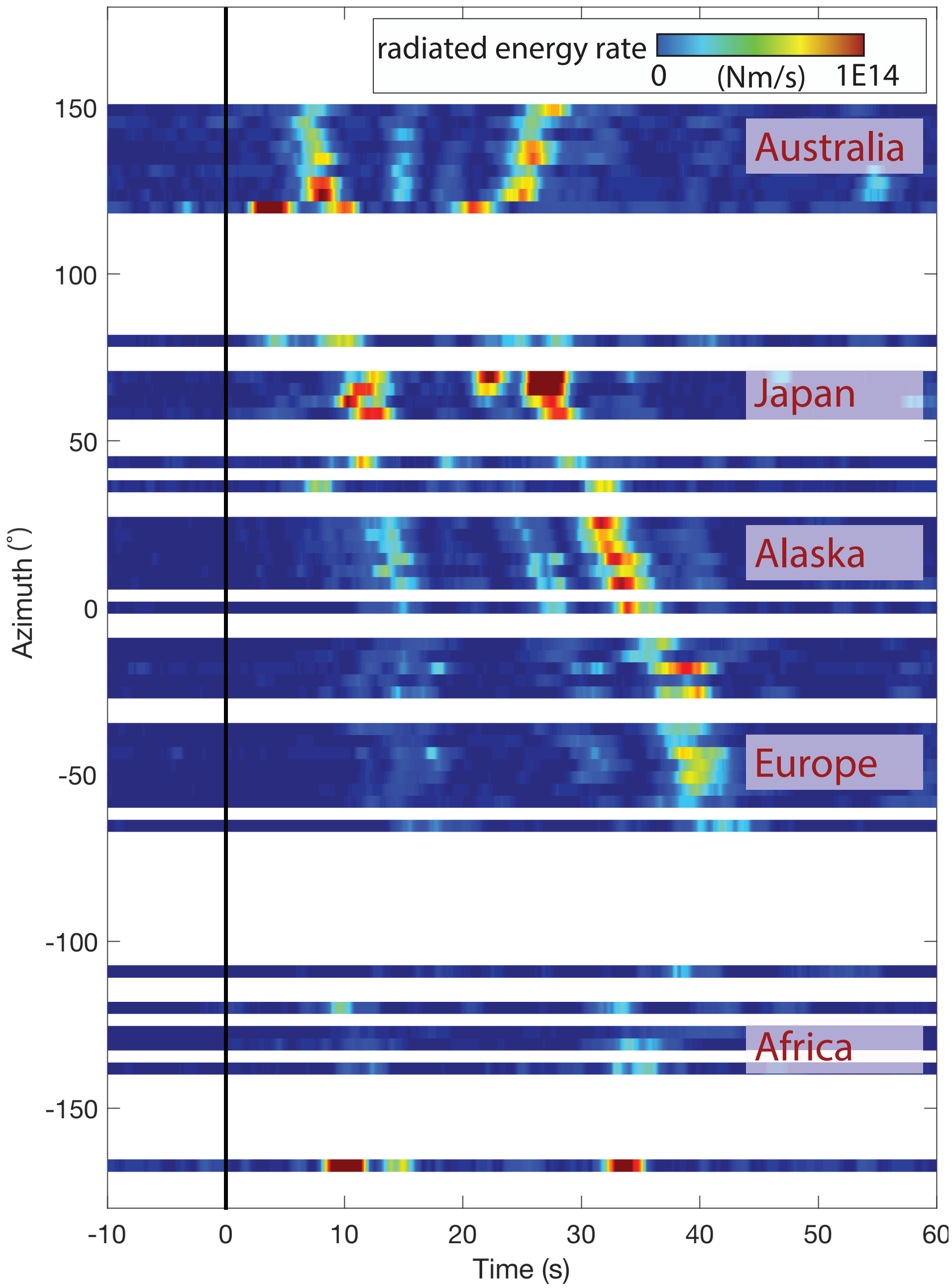


**Figure 11.** Radiated energy rate across the azimuths where data is available. Colorscale denotes the strength of the radiated energy energy at a any time. The black line highlights the earthquake origin time. Approximate azimuths of regional seismic networks shown in red letters.

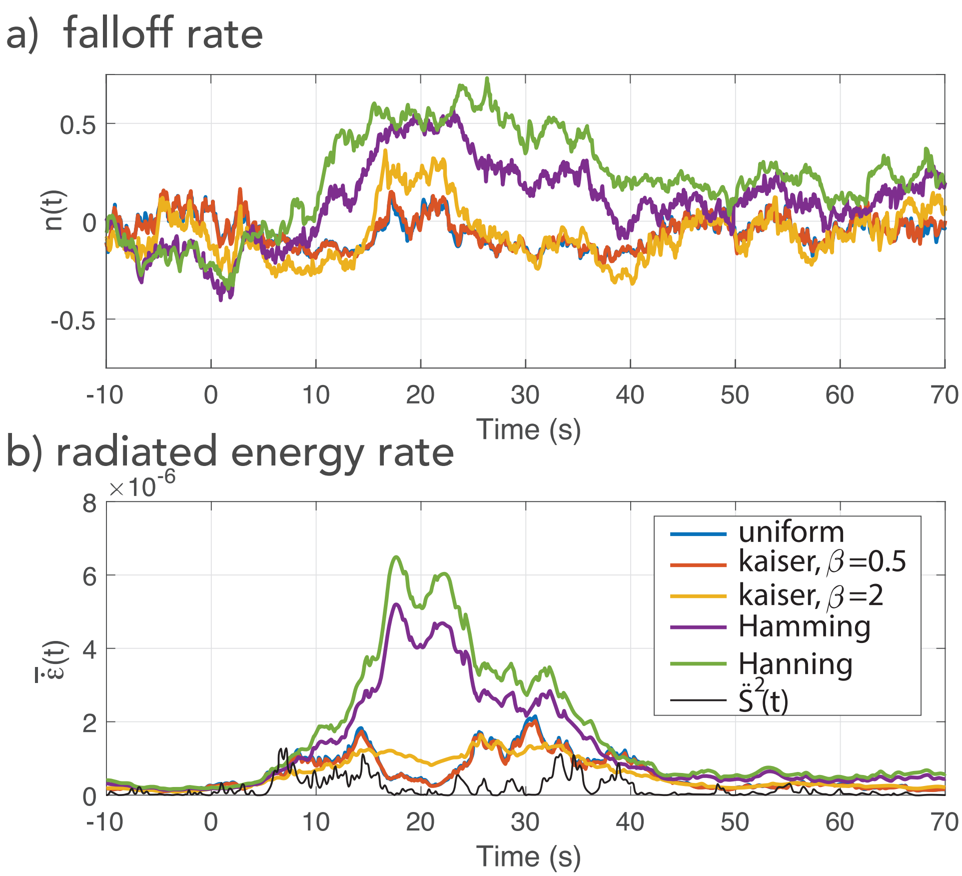


**Figure 12.** Results sensitivity to the choice of tapers: uniform tapers (no taper), Kaiser functions, Hamming, and Hanning functions on the relative high-frequency falloff rate (a) and radiated energy rate normalized to the known seismic moment from GCMT, $\bar{\dot{\varepsilon}}(t)$ (b). In (a), the mean falloff rate (e.g. the falloff rate of the taper function) between -50 and -10 s is removed.

of 0.51 E+16 J. We can scale these estimates with the GCMT seismic moment ($M_0^U$) and find that $E_R/M_0^U$ for the SCARDEC pulse is 4.43E-5, of USGS is 1.3E-4, and from our study, 5E-6. There are great implications in interpreting the radiated energy from an average STF and because independent calculations provide one order of magnitude difference, we ought to provide a more consistent time and frequency domain analysis of the P-wave source pulse.

### 4.6 On pulse duration estimates

We validate duration estimates using both STF and $\dot{\varepsilon}(t)$ functions, stacked over azimuth and shown in Figure 13. The duration from centroid time $T_C$ is

$$T_C = \frac{\int_0^\infty F(t)tdt}{\int_0^\infty F(t)dt}, \tag{19}$$

where $F(t)$ is either $\dot{S}(t)$ or $\dot{\varepsilon}(t)$ and $\int_0^\infty F(t)dt$ represents either the moment or the radiated energy. Centroid times are half a duration that is weighted by the moment-rate function. They are reasonable duration estimates if the function $F(t)$ is symmetric in time. Because both stacked $\dot{S}(t)$ or $\dot{\varepsilon}(t)$ are relatively symmetric, the duration estimated from the centroid times match reasonably well, 45.89 s and 50.25 s, respectively. Rayleigh-wave derived STFs provide a median duration of 72 s (IRIS automated product), the GCMT provides a duration of 62.4 s. The difference between our centroid times and those found using Rayleigh waves may arise from the low radiation of P waves in the first 10 s of the rupture.

Another estimate of duration heightens the contribution of the time variable in the integral as compared to the moment-based duration (centroid time) and is calculated from the second moment [*McGuire et al.*, 2002],

$$T_M = 2\sqrt{\frac{\int_0^\infty F(t)t^2dt}{\int_0^\infty F(t)dt}}. \tag{20}$$

Note that neither centroid times nor second moments have been calculated using radiated energy rate in the past, and thus we treat them simply as weighted time averages. Using the stacked $\dot{S}(t)$ or $\dot{\varepsilon}(t)$ functions, we find that a duration of 49.23 or 54.8 also provide reasonable durations, values that are closer to published duration estimates [*Yagi and Okuwaki*, 2015; *Yue et al.*, 2017].

We also explore the choice of a threshold after which the amplitudes become lower than the peak amplitudes of the function. We choose 5% as a threshold following *Persh and Houston* [2004]. We find a duration for $\dot{S}(t)$ of 50.05 s and 46.27 s for $\dot{\varepsilon}(t)$. Because the Nepal earthquake was a unilateral rupture and a shallow dipping fault, variations in pulse width may reliable indicate rupture velocity [*Park and Ishii*, 2013]. Figures 11 and 14 exhibit clear modulation of the pulse duration, ranging from 30 s up to 45 s. We attempt these duration metrics (centroid time, second moment, threshold-based duration) to establish the azimuthal variations in pulse durations. We also estimate the duration from corner frequencies given a double-corner frequency model [*Haskell*, 1964; *Kane et al.*, 2013; *Denolle and Shearer*, 2016] and a stretching technique [*Prieto et al.*, 2017] to calculate relative durations. We use the STF, radiated energy rate functions, and the product of both to increase signal to noise ratio. Supplementary materials Figure S11 show the variations of the estimate with azimuth, none of which provide stable results. We conclude that the moment-rate and moment acceleration weighted times (centroid and second moments) rely on a functional shapes that are symmetric with regard to the half duration in order to provide a reliable results. While the stacked functions appear symmetric, individual pulses exhibit clear features that likely shift the centroid or second moment time either earlier or after the half duration. In particular, the arrest of the rupture appear more energetic than

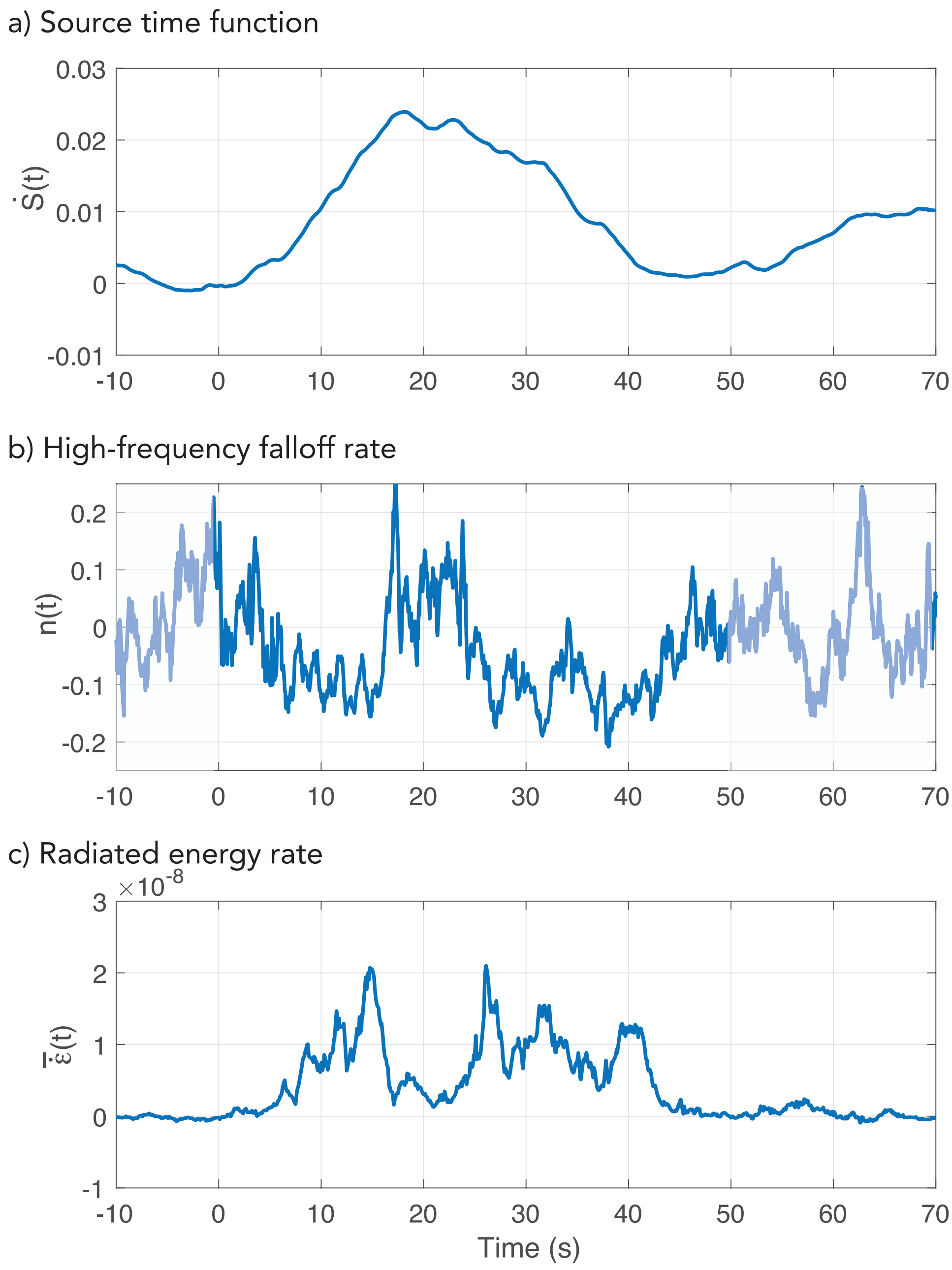


**Figure 13.** Similar to Figure 7 for the observed case of the M7.8 2015 Nepal earthquake: (a) STF normalized to $M_0^U$, (b) falloff rate function, and (c) radiated energy rate function normalized to $M_0^U$, all averaged over azimuthal bins. Interpretations of the moment acceleration and deceleration in terms of evolution of $n(t)$ and $\dot{\varepsilon}(t)$ follows similar notation as in Figure 2.

the slip onset, thus the weighted integral is forcing the centroid time and second moment to be late in the rupture. Consequently, twice the centroid time yields an overestimate of the pulse duration.

### 4.7 Discussion on radiated energy rate

The evolution of radiated energy rate is not uniform. Because it is sensitive to high frequency seismic waves, it can easily be interpreted in term of spatial locations with teleseismic backprojection. We organize this discussion along three main stages of the rupture: the initiation, propagation, and deceleration phases.

The rupture initiation occurs over 10-20 s and radiated very little seismic energy. Analysis of teleseismic backprojection (BP) agree with this finding [*Fan and Shearer*, 2015; *Yagi and Okuwaki*, 2015; *Avouac et al.*, 2015; *Meng et al.*, 2016]. Other backprojection studies also make the observation that the first 20 s of the events were focused on the hypocentral zone. It is worth discussing that the onset of the rupture is characterized by an almost linear growth of the moment rate function with time: the STF is linear from 0 to 10-15 s. This growth is weaker than that predicted by cracks with constant rupture velocity [*Sato and Hirasawa*, 1973], it is also weaker than observed by other crustal earthquakes [*Meier et al.*, 2016].

The main rupture propagation between moment acceleration and deceleration is characterized by a period of weak radiation. It is expected from a simple moving dislocation model, as discussed in our canonical example. Source directivity stretches considerably the source pulse and thus any interpretation of temporal radiation on the fault plane relies on results from BP studies. Different seismic networks provide different BP images as expected by the modulation of the source pulse with directivity. A clear example is shown by *Zhang et al.* [2016], whereby the timing of weak radiation, seen either by Europe (azimuths $\sim$ -50°, $t$ = 20 – 35 s) or Australia (azimuths $\sim$ 120°, $t$ = 10 – 25 s) or Alaskan (azimuths $\sim$ 20°, $t$ = 20 – 30 s) arrays, coincides in time and space where most of the slip was released. The propagation of the rupture is interpreted by *Yue et al.* [2017] as being mostly uniform with little variation in rupture velocity that would generate high frequency radiation. It is also that of greatest slip and is located underneath Kathmandu. There are distinct events of high-frequency radiation within this quiet time, in particular just before the deceleration phase. One possible interpretation is the role of the fault geometry in rupture propagation. Ruptures that propagate through kinks radiated high frequency waves and alter the radiated energy rate [*Adda-Bedia and Madariaga*, 2008]. *Denolle et al.* [2015] and *Hubbard et al.* [2016] suggested that lateral ramps must affect the rupture propagation and likely confine the slip zone.

The rupture is expected to decelerate around 30 - 40 s. Our results suggest that the arrest of the rupture is more energetic than the onset with maximum radiated energy and is visible at all azimuths (Fig. 11). Rupture deceleration is also proposed by *Yagi and Okuwaki* [2015] to generate high-frequency radiation. Focusing now on azimuth 60°, where we estimate a strong radiation that coincides with a particularly energetic pulse at 30 s (Fig. 10). This azimuth points towards the down-dip end of the MHT, where the two aftershocks are located. The whole-event displacement Fourier amplitude spectra exhibit also an elevated level around 0.1 – 0.2 Hz (see Fig. S20). It is worth pointing to the result of *Yue et al.* [2017], who note an acceleration of the propagation towards the eastern down-dip end of the fault (azimuth $\sim$ 50° from the earthquake centroid location).

### 4.8 Discussion on total radiated energy

There are several approaches to estimating the radiated energy. To strictly follow the definition that the total radiated energy is the integral of the energy flux through a far-field sphere (*Haskell* [1964], equations (15) and (16) and *Boatwright* [1980] equation (11)), one has to integrate the contributions of the radiated energy over the focal sphere. We ignore the longitudinal dimension of the focal sphere (i.e. takeoff angles) because we have incorporated contributions of some global and depth phases in the radiated energy pulse. However, we follow the integral over azimuths.

At each point of the focal sphere, equation (11) of *Boatwright* [1980] shows that the total radiated energy is the integral over time of the radiated energy rate. Applying Parseval's theorem, it is strictly equivalent to estimating radiated energy using the squared velocity source spectra, which we refer to as "whole-spectrum based" radiated energy in Figure 14. This measure of total radiated energy is a much more popular approach [*Baltay et al.*, 2014; *Denolle et al.*, 2015]. Thus, the correct method to estimate radiated energy is based on a representation of either radiated energy rate functions or source spectra in azimuth bins. We choose to average the time-domain functions within the bins and to take the median of the spectral shape (assuming that they are log-normally distributed). If we had a greater sampling at each azimuth bins, more rigorous pooling techniques could provide statistical estimates of the functions and spectra. There are other ways to estimate radiated energy, though they are mathematically less correct. For instance, we can average the radiated energy values within each azimuth bins. These averages are slightly larger than those from the previous approach, which we expect from a log-normal distribution of energy values.

The total radiated energy is not isotropic with azimuth, as some directions experience 7 times more seismic energy than others. Azimuthal variations in radiated energy is clearly dominated by source directivity. The most energetic direction is that of the propagating pulse around 100°. The estimates from the time-domain squared moment accelerations are systematically lower than the other estimates by a factor of about 2, which was a second argument against using the time domain approach. The whole-spectrum and radiated energy based estimates are quite consistent with each other, well within a factor of 2.

To compare with other studies, we make the assumption that the S-source pulses are identical to the P-source pulses such that the ratio between S and P energies is controlled by the difference in geometrical spreading. This approximation is common [*Convers and Newman*, 2011; *Denolle et al.*, 2015; *Denolle and Shearer*, 2016; *Ye et al.*, 2016], yet potentially introducing a bias if both pulses are different [*Hanks*, 1981; *Prieto et al.*, 2004]. We thus scale the P-wave radiated energy to that of the potential S-wave radiated energy (23.4 times in a Poisson medium where $V_P = \sqrt{3}V_S$) and sum both to estimate a total radiated energy. We obtain a total of 1.42E+16 J for the radiated energy-based estimate, which our preferred estimate given the methodology choices discussed above. These values are lower than both *Denolle et al.* [2015] (5.8E+16 J) and *Denolle and Shearer* [2016] (1.1E+17 J), but greater than those automated by IRIS (7.3 E+15 J).

If we were to consider the spread in estimates illustrated in Figure 14 as epistemic uncertainties, values can be as low as 8.0 E+15 J. Scaling the total radiated energy estimate with the GCMT moment yields a scaled energy of 1.83E-5, barely above the global median for thrust earthquakes of 1.7 E-5 [*Denolle and Shearer*, 2016]. Choosing our estimate of moment instead of the GCMT estimate would increase the scaled energy (factor of about 2). However, we believe that the GCMT moment is more representative of the total slip than ours that is derived solely from P waves. Multiplying the scaled energy with a rigidity of 4.5E10 Pa yields a value of apparent stress of $\tau_a = 0.83$ MPa [*Wyss and Brune*, 1968].

### 4.9 On the temporal variations in high-frequency falloff rates

As we have previously discussed in the canonical and kinematic examples, the interpretation of variations in high-frequency falloff rate is rather complex and may not be that informative. The evolution is however coherent across azimuths (Fig. S16) in ways

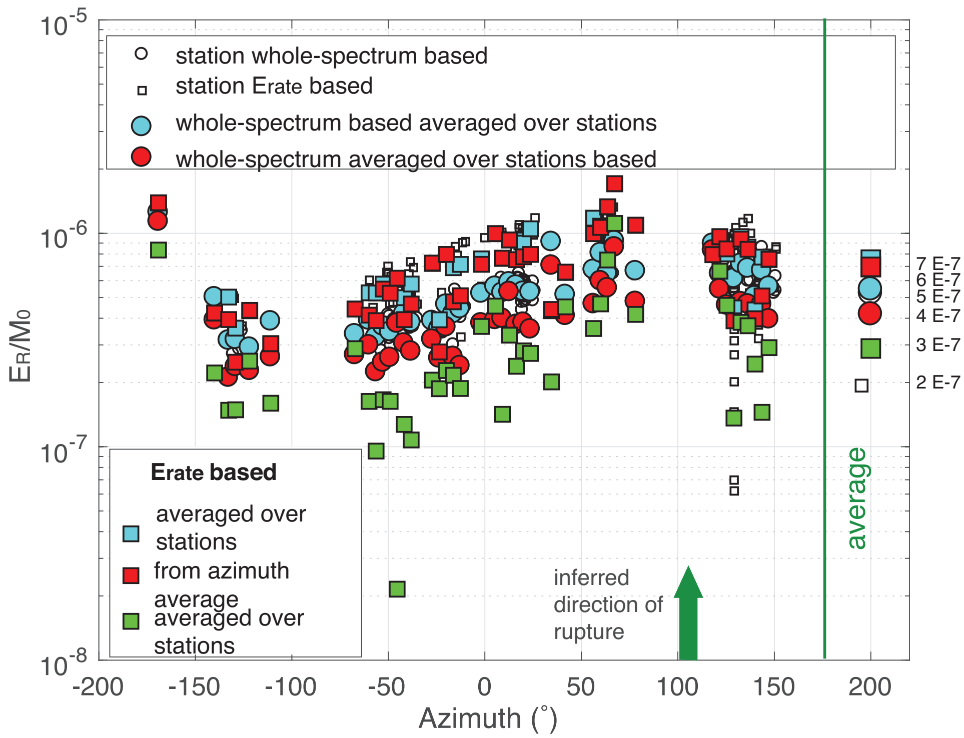


**Figure 14.** P-wave radiated energy estimates scaled by the total GCMT moment, across azimuths and their azimuthal averages. The circles reflect the values calculated from the whole-pulse source spectrum, the squares reflect those calculated from the time integral of the radiated energy rate. Open markers reflect the values at each stations, blue markers indicate the energy values averaged over stations in each azimuth bins, red markers show the energy values calculated from either the source spectrum or the radiated energy rate averaged over stations in each azimuth bins. Green colors reflect the energy calculated from time-domain squared moment acceleration. Green arrow indicates where the source directivity is inferred.

that seem to follow effects in the ASTF and radiated energy rate of source directivity. The values are overall low during the time of high radiation and high during the times of low radiation.

## 5 Conclusions

This study evaluates the reliability in interpreting source spectrograms and of high-frequency radiation buried in the source time function of large earthquakes. It builds upon the strengths of the spectral observations, such as the practical empirical Green's function approach that removes 3D wave propagation effects. It supplements such analysis with a rigorous calculation of the radiated energy rate emitted at different azimuths of the source. This provides a temporal evolution of the radiated energy, one that is more interpretable in terms of earthquake dynamics. We use canonical functions (such as the unilateral moving dislocation source) and statistical kinematic sources to establish that:

1. the radiated energy rate is proportional to the moment acceleration squared and is controlled by high peak slip rates and changes in rupture velocities,
2. the temporal evolution of the high frequency falloff rate is complex and only indicative of a sign change in the moment acceleration.

We further examine the effects of drastic changes in slip-rate functions on the source spectrogram, as modeled by simulations of dynamic ruptures, and find that they only alter the radiated energy rate and have no noticeable effect on the high-frequency falloff rate. We also discuss that tapering the short windows of the spectrogram, as used in *Denolle et al.* [2015] and *Yin et al.* [2018], greatly impacts the shape of the radiated energy rate function and conclude that a pure spectrogram with no taper is the best approach.

We apply this to the M7.8 2015 Nepal earthquake. We construct ASTFs across azimuths with 200 high-quality P-wave records from pure and simple deconvolution with empirical Green's functions. The ASTFs reflect strong directivity effects and we discuss their validity in terms of pulse duration and moment estimates. The radiated energy rate derived from these ASTFs confirms that the Nepal earthquake was overall well described by a Haskell model, whereby radiation is at the beginning and at the end of the rupture. We also confirm results from other studies that the rupture initiation was particularly weak in radiation and find that rupture deceleration appears to be a lot more energetic than its acceleration.

From the practical example of building ASTF and the radiated energy rate functions, we find that:

1. measuring duration (centroid moment, second moment, waveform stretching, ...) is quite difficult and not appropriate if the function is not symmetric,
2. radiated energy rate from moment acceleration squared is possible to interpret if the time-domain ASTF is of high quality and at all frequencies,
3. radiated energy rate is highly correlated in time with results from backprojection and thus provides pathway toward interpreting radiation with physical processes on the fault,
4. large slip (moment release) does not necessarily mean strong ground motion,
5. it is challenging to obtain consistent time- and frequency-domain estimate of the moment-rate function, but our approach provides a compromise between both that respects both kinematics and dynamics.

The possible interpretation of acceleration seismograms in terms of kinematic evolution of rupture is not new. *Spudich and Frazer* [1984] propose to use accelerations to infer changes in rupture velocity for near-source measurements. Apart from the specific situation of nearby measurements, an accurate estimate of the Green's function is necessary to properly remove the 3D wave propagation effects in particular when attenuation is strong and where the direct P-wave pulse is masked by scattering.

The study limited the application to P-wave pulses, but should be extended to S-wave pulses because they carry most of the seismic radiated energy. This method remains close to the data with limited processing. Because STFs are usually regularized and potentially biased, this approach brings a new observation tool to explore the broadband seismic radiation of earthquakes. The metric of radiated energy rate (seismic power) is output from dynamic rupture simulations and can validate physical models. Radiation is neither spatially isotropic nor it is uniform during the rupture. This confirms that seismic radiation ought to be better understood for accurate predictions of ground motion.

Observational seismology faces the challenge to make measurements of the earthquake at all frequencies in a self-consistent fashion. Through careful observations of recent large earthquakes, and now quantified in this study, it has become clear that the large release of seismic moment affect the long periods but that the rate and acceleration of that release controls the radiated energy and ultimately, the ground motions. The kinematic inversions of slip focus on reproducing the moment-rate function, which is best captured by geodetic measurements or long period period seismic waves. Because static displacements and long period seismic waves are not as strongly affected by 3D structure, theoretical Green's function are used to perform such kinematic inversion. Key dynamic properties of the rupture, however, are only captured by short period seismic waves, which are particularly affected by 3D structure and thus can be inferred reliably through accurate and empirical knowledge of wave propagation effects. Future endeavor lies in providing a self-consistent kinematic and dynamic view of the earthquake in order to capture the processes that lead to earthquake rupture.

## Acknowledgments

This work benefited from discussions with Chen Ji, Jean-Paul Ampuero, and with Jiuxun Yin. Data of the Nepal earthquake sequence was downloaded through the FDSN data services for the seismic networks (TM, MY, JP, IM, GB, AU, 10.7914/SN/TA, 10.13127/SD/fBBBtDtd6q, 10.7914/SN/IU, 10.7914/SN/II, 10.7914/SN/IC10.7914/SN/GT,10.14470/TR560404, 10.18715/GEOSCOPE.G, 10.7914/SN/CZ, 10.7914/SN/CN, 10.12686/sed/networks/ch, 10.1785/0120090257, 10.7914/SN/AK, 10.7914/SN/AF, 10.7914/SN/AT). Data products such as duration and GCMT estimated were extracted from IRIS derived products. IRIS Data Services are funded through the Seismological Facilities for the Advancement of Geoscience and EarthScope (SAGE) Proposal of the National Science Foundation under Cooperative Agreement EAR-1261681.

## References

Abercrombie, R. E. (1995), Earthquake locations using singleâĂŘstation deep borehole recordings: Implications for microseismicity on the San Andreas fault in southern California, *J. Geophys. Res. Solid Earth*, *100*(B12), 24,003–24,014.

Abercrombie, R. E. (2015), Investigating uncertainties in empirical Green's function analysis of earthquake source parameters, *J. Geophys. Res. Solid Earth*, *120*(6), 4262–4277, doi:10.1002/2015JB011984.

Abercrombie, R. E., S. Bannister, J. Ristau, and D. Doser (2016), Variability of earthquake stress drop in a subduction setting, the Hikurangi Margin, New Zealand, *Geophys. J. Int.*, *208*, 306–320, doi:10.1093/gji/ggw393.

Adda-Bedia, M., and R. Madariaga (2008), Seismic radiation from a kink on an antiplane fault, *B. Seismol. Soc. Am.*, *98*(5), 2291–2302.

Aki, K., and P. G. Richards (2002), *Quantitative Seismology, Second Edition*, 700 pp., University Science Books, Sausalito, California.

Allmann, B. P., and P. M. Shearer (2009), Global variations of stress drop for moderate to large earthquakes, *J. Geophys. Res.*, *114*, B01,310.

Avouac, J.-P., L. Meng, S. Wei, T. Wang, and J.-P. Ampuero (2015), Lower edge of locked main himalayan thrust unzipped by the 2015 gorkha earthquake, *Nature Geosci*, *advance online publication*, –.

Baltay, A. A., G. A. Prieto, and G. C. Beroza (2010), Radiated seismic energy from coda measurements and no scaling in apparent stress with seismic moment, *J. Geophys. Res.*, *115*, B08,314.

Baltay, A. A., G. C. Beroza, and S. Ide (2014), Radiated energy of great earthquakes from teleseismic empirical Green's function deconvolution, *Pure and Applied Geophysics*, *171*(10), 2841–2862.

Bertero, M., D. Bindi, P. Boccacci, M. Cattaneo, C. Eva, and V. Lanza (1997), Application of the projected Landweber method to the estimation of the source time function in seismology, *Inverse Problems*, *13*, 465–486.

Boatwright, J. (1980), A spectral theory for circular seismic sources; simple estimates of source dimension, dynamic stress drop, and radiated energy, *B. Seismol. Soc. Am.*, *70*(1), 1–27.

Brown, L., K. Wang, and T. Sun (2015), Static stress drop in the $M_w$ 9 Tohoku-oki earthquake: heterogeneous distribution and low average value, *Geophys. Res. Lett.*, *42*(24), 10,595–10,600, doi:10.1002/2015GL066361.

Bruhat, L., Z. Fang, and E. M. Dunham (2016), Rupture complexity and the supershear transition on rough faults, *J. Geophys. Res. Solid Earth*, *121*(1), 210–224, doi: 10.1002/2015JB012512.

Chounet, A., M. Vallée, M. Causse, and F. Courboulex (2017), Global catalog of earthquake rupture velocities shows anticorrelation between stress drop and rupture velocity, *Tectonophysics*, doi:10.1016/j.tecto.2017.11.005.

Cochard, A., and R. Madariaga (1994), Dynamic faulting under rate-dependent friction, *PAGEOPH*, *142*(3-4), 419–445, doi:10.1007/BF00876049.

Convers, J. A., and A. V. Newman (2011), Global evaluation of large earthquakes energy from 1997 through mid-2010, *J. Geophys. Res.*, *116*, B08,304.

Crempien, J. G. F., and R. J. Archuleta (2015), Ucsb method for simulation of broadband ground motion from kinematic earthquake sources, *Seismol. Res. Lett.*, *86*(1).

Crotwell, H. P., T. J. Owens, and J. Ritsema (1999), The TauP toolkit: Flexible seismic travel-time and ray-path utilities, *Seismol. Res. Lett.*, *70*(2), 154–160.

Das, S., and K. Aki (1977), Fault plane with barriers: A versatile earthquake model, *J. Geophys. Res. Solid Earth*, *82*(36), 5658–5670, doi:10.1029/JB082i036p05658.

Day, S. (1982), Three-dimensional finite difference simulation of fault dynamics: rectangular faults with fixed rupture velocity, *B. Seismol. Soc. Am.*, *72*(3), 705–727.

Denolle, M. A., and P. M. Shearer (2016), New perspectives on selfâĂŘsimilarity for shallow thrust earthquakes, *J. Geophys. Res.*, *121*(9), 6533–6565.

Denolle, M. A., W. Fan, and P. M. Shearer (2015), Dynamics of the 2015 m7.8 nepal earthquake, *Geophysical Research Letters*, *42*(18), 7467–7475.

Dunham, E. M., D. Belanger, L. Cong, and J. E. Kozdon (2011), Earthquake ruptures with strongly rate-weakening friction and off-fault plasticity, part 2: Nonplanar faults, *B. Seismol. Soc. Am.*, *101*(5), 2308–2322, doi:10.1785/0120100076.

Duputel, Z., J. Vergne, L. Rivera, G. Wittlinger, V. Farrra, and G. Hetényi (2016), The 2015 Gorkha earthquake: a large event illuminating the Main Himalayan Thrust fault., *Geophys. Res. Lett.*, *43*(6), 2517–2525.

Ekström, G., M. Nettles, and A. M. Dziewonski (2012), The global CMT project 2004-2010: Centroid-moment tensors for 13,017 earthquakes, *Phys. Earth Planet. In.*, *200-201*, 1–9.

Fan, W., and P. M. Shearer (2015), Detailed rupture imaging of the 25 April 2015 Nepal earthquake using teleseismic P waves, *Geophys. Res. Lett.*, *42*(14), 5744–5752.

Galetzka, J., D. Melgar, J. F. Genrich, J. Geng, S. Owen, E. O. Lindsey, X. Xu, Y. Bock, J. P. Avouac, L. B. Adhikari, B. N. Upreti, B. Pratt-Sitaula, T. N. Bhattarai, B. P. Sitaula, A. Moore, K. W. Hudnut, W. Szeliga, J. Normandeau, M. Fend, M. Flouzat, L. Bollinger, P. Shrestha, B. Koirala, U. Gautam, M. Bhatterai, R. Gupta, T. Kandel, C. Timsina, S. N. Sapkota, S. Rajaure, and N. Maharjan (2015), Slip pulse and resonance of Kathmandu basin during teh 2015 Mw 7.8 Gorkha earthquake, Nepal imaged with geodesy, *Sciencexpress*.

Galvez, P., J.-P. Ampuero, L. A. Dalguer, S. N. Somala, and T. Nissen-Meyer (2014), Dynamic earthquake rupture modelled with an unstructured 3-d spectral element method applied to the 2011 M 9 Tohoku earthquake, *Geophys. J. Int.*, *198*(2), 1222–1240.

Graves, R. W., and A. Pitarka (2016), GroundâĂŘmotion simulations on rough faults including effects of 3d stochastic velocity perturbations, *B. Seismol. Soc. Am.*, *106*(5), 2136–2153, doi:10.1785/0120160088.

Guatteri, M., and P. Spudich (2000), What can strong-motion data tell us about slip-weakening fault-friction laws?, *B. Seismol. Soc. Am.*, *90*(1), 98–116, doi: 10.1785/0119990053.

Guatteri, M., P. M. Mai, and G. C. Beroza (2004), A Pseudo-Dynamic Approximation to Dynamic Rupture Models for Strong Ground Motion Prediction, *B. Seismol. Soc. Am.*, *94*(6), 2051–2063.

Hanks, T. C. (1981), The corner frequency shift, earthquake source models, and q, *B. Seismol. Soc. Am.*, *71*(3), 597–612.

Haskell, N. A. (1964), Total Energy and Energy Spectral Density of Elastic Wave Radiation from Propagatin Faults, *B. Seismol. Soc. Am.*, *54*(6), 1811–1841.

Hayes, G. P. (2017), The finite, kinematic rupture properties of great-sized earthquakes since 1990, *Earth Planet. Sc. Lett.*, *468*, 94–100, doi:10.1016/j.epsl.2017.04.003.

Houston, H. (2001), Influence of depth, focal mechanism, and tectonic setting on the shape and duration of earthquake source time functions, *J. Geophys. Res.*, *106*(B6), 11,137–11,150.

Huang, Y., L. Meng, and J.-P. Ampuero (2013), A dynamic model of the frequency-dependent rupture process of the 2011 tohoku-oki earthquake, *Earth, Planets and Space*, *64*(12), 1, doi:10.5047/eps.2012.05.011.

Hubbard, J., R. Almeida, A. Foster, S. N. Sapkota, P. Bürgi, and P. Tapponnier (2016), Structural segmentation controlled the 2015 Mw 7.8 Gorkha earthquake rupture in Nepal, *Geology*, *44*(8), 639–642, doi:10.1130/G38077.1.

Ide, S., K. Imanishi, Y. Yoshida, G. C. Beroza, and D. Shelly (2008), Bridging the gap between seismically and geodetically detected slow earthquakes, *Geophys. Res. Lett.*, *35*(10), doi:10.1029/2008GL034014.

Ide, S., A. A. Baltay, and G. C. Beroza (2011), Shallow dynamic overshoot and energetic deep rupture in the 2011 $M_w$ 9.0 Tohoku-Oki earthquake, *Science*, *332*(6036), 1426–1429.

Ihmlé, P. (1998), On the interpretation of subevents in telseismic waveforms: the 1994 Bolivia deep earthquake revisited, *J. Geophys. Res.*, *103*(B8), 17,919–17,932.

Ihmlé, P., and T. H. Jordan (1995), source time function of the great 1994 Bolivia deep earthquake by waveform and spectral inversions, *Geophys. Res. Lett.*, *22*(16), 2253–2256.

Ji, C., D. J. Wald, and D. V. Helmberger (2002), Source description of the 1999 hector mine, california, earthquake, part i: Wavelet domain inversion theory and resolution analysis, *B. Seismol. Soc. Am.*, *92*(4), 1192–1207, doi:10.1785/0120000916.

Kaimal, J. C., and L. Kristensen (1991), Time series tapering for short data samples, *Boundary-Layer Metorology*, *57*(1), 187–194.

Kanamori, H., and L. Rivera (2006), *Energy partitioning during an earthquake*, American Geophysical Union, Washington, doi:10.1029/170GM03.

Kane, D. L., D. L. Kilb, and F. L. Vernon (2013), Selecting Empirical Green's Functions in Regions of Fault Complexity: A Study of Data From the San Jacinto Fault Zone, Southern California, *B. Seismol. Soc. Am.*, *103*(2A).

Kennett, B. L. N., and E. R. Engdahl (1991), *IASPEI 1991 Seismological Tables*, Bibliotech, Canberra, Australia.

Kikuchi, M., and H. Kanamori (1991), Inversion of complex body waves - iii, *B. Seismol. Soc. Am.*, *81*(6), 2335–2350.

Kostrov, B. V. (1964), Selfsimilar problems of propagation of shear cracks, *Journal of Applied Mathematics and Mechanics*, *28*(5), 1077–1087, doi:10.1016/0021-8928(64)90010-3.

Kozdon, J. E., and E. M. Dunham (2013), Rupture to the trench: Dynamic rupture simulations of the 11 March 2011 Tohoku eartqhauek, *B. Seismol. Soc. Am.*, *103*, 1275–1289.

Lay, T., L. Ye, K. D. Koper, and H. Kanamori (2017), Assessment of teleseismically-determined source parameters for the April 25 015 $M_w$ 7.9 Gorkha, Nepal earthquake and the May 12, 2015 $M_w$ 7.2 aftershock, *Tectonophysics*, *714*, 4–20.

Liu, P., R. J. Archuleta, and S. Hartzell (2006), Prediction of broadband ground-motion time histories: hybrid low/high- frequency method with correlated random source parameters, *B. Seismol. Soc. Am.*, *96*(6), 20,118–2130.

Longuet-Higgins, M. S. (1950), A Theory of the Origin of Microseisms, *Philos. Tr. R. Soc. S.-A.*, *243*, 1–35.

Lotto, G. C., E. M. Dunham, T. N. Jeppson, and H. J. Tobin (2017), The effect of compliant prisms on subduction zone earthquakes and tsunamis, *Earth Planet. Sc. Lett.*, *458*, 213–222, doi:10.1016/j.epsl.2016.10.050.

Ma, S., and E. T. Hirakawa (2013), Dynamic wedge failure reveals anomalous energy radiation of shallow subduction eartquakes, *Earth Planet. Sc. Lett.*, *375*, 113–122.

Madariaga, R. (1983), High frequency radiation from dynamic earthquake, *Ann. Geophys*, *1*, 17–23.

Mai, P. M., and G. C. Beroza (2000), Source Scaling Properties from Finite-Fault-Rupture Models, *B. Seismol. Soc. Am.*, *90*(3), 604–615.

McGuire, J. J. (2004), Estimating finite source properties of small earthquake ruptures, *B. Seismol. Soc. Am.*, *94*(2), 377–393.

McGuire, J. J. (2017), A MATLAB toolbox for estimating the second moments of earthquake ruptures, *Seismol. Res. Lett.*, *88*(2A), 371–378.

McGuire, J. J., L. Zhao, and T. H. Jordan (2002), Predominance of unilateral rupture for a global catalog of large earthquakes, *B. Seismol. Soc. Am.*, *92*(8), 3309–3317, doi: 10.1785/0120010293.

Meier, M.-A., T. H. Heaton, and J. Clinton (2016), Evidence for universal earthquake rupture initiation behavior, *Geophys. Res. Lett.*, *43*(15), 7991–7996, doi: 10.1002/2016GL070081.

Meier, M.-A., J.-P. Ampuero, and T. H. Heaton (2017), The hidden simplicity of subduction megathrust earthquakes., *Science*, *357*(6357), 1277–1281.

Meng, L., A. Inbal, and J.-P. Ampuero (2011), A window into the complexity of the dynamic rupture of the 2011 Mw 9 Tohoku-Oki earthquake, *Geophys. Res. Lett.*, *38*, L00G07.

Meng, L., A. Zhang, and Y. Yagi (2016), Improving back projection imaging with a novel physicsâĂŘbased aftershock calibration approach: A case study of the 2015 Gorkha earthquake, *Geophys. Res. Lett.*, *43*(2), 628–636, doi:10.1002/2015GL067034.

Nissen-Meyer, T., M. V. Driel, S. C. Stähler, K. Hosseimi, S. Hempel, L. Auer, A. Colombi, and A. Fournier (2014), Axisem: broadband 3-d seismic wavefields in axisymmetric media, *Solid Earth*, *5*, 425–445, doi:10.5194/se-5-425-2014.

Noda, H., N. Lapusta, and H. Kanamori (2013), Comparison of average stress drop measures for ruptures with heterogeneous stress change and implications for earthquake physics, *Geophys. J. Int.*, *193*, 1691–1712.

Ohnaka, M., and Y. Kuwahara (1990), Characteristic features of local breakdown near a crack-tip in the transition zone from nucleation to unstable rupture during stick-slip shear failure, *Tectonophysics*, *175*(1-3), 197–220, doi:10.1016/0040-1951(90)90138-X.

Park, S., and M. Ishii (2013), Inversion for rupture properties based upon 3-D directivity effect and application to deep earthquakes in the Sea of Okhotsk region, *Geophys. J. Int.*, *203*(2), 1011–1025, doi:10.1093/gji/ggv352.

Pérez-Campos, X., and G. C. Beroza (2001), An apparent mechanism dependence of radiated seismic energy, *J. Acoust. Soc. of Am.*, *106*(B6), 11,127–11,136.

Persh, S. E., and H. Houston (2004), Deep earthquake rupture histories determined by global stacking of broadband p waveforms, *J. Geophys. Res. Solid Earth*, *109*(B4), 2156–2202.

Poli, P., and G. A. Prieto (2016), Global rupture parameters for deep and intermediate-depth earthquakes, *J. Geophys. Res. Solid Earth*, *121*(12), 8871–8887.

Prieto, G. A., P. M. Shearer, F. L. Vernon, and D. L. Kilb (2004), Earthquake source scaling and self-similarity estimation from stacking P and S spectra, *J. Geophys. Res.*, *109*, B08,310.

Prieto, G. A., R. L. Parker, and F. L. V. III (2009), A Fortan 90 library for mutlitaper spectrum analysis, *Comput. Geosci.*, *35*, 1701–1710, doi:10.1016/j.cageo.2008.06.007.

Prieto, G. A., B. Froment, C. Yu, and R. E. Abercrombie (2017), Earthquake rupture below the brittle-ductile transition in continental lithospheric mantle, *Science Advances*, *3*(3), e1602,642, doi:10.1126/sciadv.1602642.

Ross, Z. E., and Y. Ben-Zion (2016), Toward reliable automated estimates of earthquake source properties from body wave spectra, *J. Geophys. Res. Solid Earth*, *121*(6), 4390–4407.

Roten, D., K. B. Olsen, S. M. Day, Y. Cui, and D. Fäh (2014), Expected seismic shaking in los angeles reduced by San Andreas fault zone plasticity, *Geophys. Res. Lett.*, *41*, 2769–2777.

Roten, D., K. B. Olsen, S. M. Day, and Y. Cui (2017), Quantification of fault zone plasticity effects with spontaneous rupture simulations, *Pure and Applied Geophysics*, *174*(9), 3369–3391.

Sato, H., and T. Hirasawa (1973), Body wave spectra from propagating shear cracks, *J. Appl. Phy. of the Earth*, *84*, 829–841.

Schmedes, J., R. J. Archuleta, and D. Lavallée (2010), Correlation of earthquake source parameters inferred from dynamic rupture simulations., *J. Geophys. Res.*, *115*(B3), 2156–2202.

Schmedes, J., R. J. Archuleta, and D. Lavallée (2013), A kinematic rupture model generator incorporating spatial interdependency of earthquake source parameters, *Geophys. J. Int.*, *192*, 1116–1131.

Shearer, P. M., G. A. Prieto, and E. Hauksson (2006), Comprehensive analysis of earthquake source spectra in southern California, *J. Geophys. Res.*, *111*, B06,303.

Spudich, P., and L. N. Frazer (1984), Use of ray theory to calculate high-frequency radiation from earthquake sources having spatially variable rupture velocity and stress drop, *B. Seismol. Soc. Am.*, *74*(6), 2061–2082.

Stockwell, R. G., L. Mansinha, and R. P. Lowe (1996), Localization of the complex spectrum: the S transform, *IEEE Trans Signal Processing*, *44*, 998–1001.

Tary, J. B., R. H. Herrera, J. Han, and M. Baan (2014), Spectral estimation: What is new? What is next?, *Rev. Geophys.*, *52*(4), 723–749.

Tinti, E., E. Fukuyama, A. Piatanesi, and M. Cocco (2005), A kinematic source-time function compatible with earthquake dynamics, *B. Seismol. Soc. Am.*, *95*(4), 1211–1223.

Trugman, D. T., and P. M. Shearer (2017), Application of an improved spectral decomposition method to examine earthquake source scaling in Southern California, *J. Geophys. Res. Solid Earth*, *122*(4), 2890–2910.

Vallée, M., J. Charléty, A. M. Ferreira, B. Delouis, and J. Vergoz (2011), Scardec: a new technique for the rapid determination of seismic moment magnitude, focal mechanism and source time functions for large earthquakes using body-wave deconvolution, *Geophys. J. Int.*, *184*(1), 338–358.

Velasco, A. A., C. J. Ammon, and T. Lay (1994), Recent large earthquakes near Cape Mendicino and in the Gorda plate: Broadband source time functions, fault orientations, and rupture complexities, *J. Geophys. Res.*, *99*(B1), 711–728.

Warren, L. M., and P. M. Shearer (2006), Systematic determination of earthquake rupture directivity and fault planes from analysis of long-period P-wave spectra, *Geophys. J. Int.*, *164*(1), 46–62, doi:10.1111/j.1365-246X.2005.02769.x.

Wirth, E. A., A. D. Frankel, and J. E. Vidale (2017), Evaluating a kinematic method for generating broadband ground motions for great subduction zone earthquakes: Application to the 2003 Mw 8.3 TokachiâĂŘOki earthquake, *B. Seismol. Soc. Am.*, *107*(4), 1737–1753, doi:10.1785/0120170065.

Wyss, M., and J. N. Brune (1968), Seismic moment, stress, and source dimensions for earthquakes in the California-Nevada region, *J. Geophys. Res.*, *73*(14), 4681–4694.

Yabe, S., and S. Ide (2014), Spatial distribution of seismic energy rate of tectonic tremors in subduction zones, *J. Geophys. Res. Solid Earth*, *119*(11), 8171–8185, doi:10.1002/2014JB011383.

Yagi, Y., and R. Okuwaki (2015), Integrated seismic source model of the 2015 Gorkha, Nepal, earthquake, *Geophys. Res. Lett.*, *42*.

Yao, H., P. G. P. M. Shearer, and C. Mecklenbräuker (2011), Compressive sensing of the TohokuâĂŘOki Mw 9.0 earthquake: FrequencyâĂŘdependent rupture modes, *Geophys. Res. Lett.*, *38*(20), L20,310, doi:10.1029/2011GL049223.

Ye, L., T. Lay, H. Kanamori, and L. Rivera (2016), Rupture characteristics of major and great ($M_w > 7.0$) megathrust earthquakes from 1990 to 2015: 1. Source parameter scaling relationships, *J. Geophys. Res.*, *121*, doi:10.1002/2015JB01246.

Yin, J., H. Yao, H. Yang, J. Liu, W. Qin, and H. Zhang (2017), Frequency-dependent rupture process, stress change, and seismogenic mechanism of the 25 April 2015 Nepal [g]orkha Mw 7.8 earthquake, *Science China Earth Sciences*, *60*(4), 796–808.

Yin, J., M. A. Denolle, and H. Yao (2018), Spatial and temporal evolution of earthquake dynamics: Case study of the Mw 8.3 Illapel earthquake, Chile, *J. Geophys. Res. Solid Earth*, doi:10.1002/2017JB014265.

Yoffe, E. H. (1951), Lxxv. the moving griffith crack, *the London, Edingurgh, and Dublin Philosophical Magazine and Journal of Science*, *42*(330), 739–750, doi:10.1080/14786445108561302.

Yue, H., M. Simons, Z. Duputel, J. Jiang, E. Fielding, C. Liang, S. Owen, A. Moore, B. Riel, J.-P. Ampuero, and S. V.Samsonov (2017), Depth varying rupture properties during the 2015 mw 7.8 gorkha (nepal) earthquake, *Tectonophysics*, *714*, 44–54, doi:10.1016/j.tecto.2016.07.005.

Zhang, H., S. Lee, and Z. Ge (2016), Multiarray rupture imaging of the devastating 2015 Gorkha, Nepal, earthquake sequence., *Geophys. Res. Lett.*, *43*(2), 584–591, doi:10.1002/2015GL066657.